IMPLEMENTATION, ASSESSMENT, AND EXTENSION OF THE WRAY-AGARWAL TURBULENCE MODEL FOR SHOCK WAVE-BOUNDARY LAYER INTERACTIONS

A THESIS SUBMITTED TO
THE GRADUATE SCHOOL OF NATURAL AND APPLIED SCIENCES
OF
MIDDLE EAST TECHNICAL UNIVERSITY

BY

SEMİH CAN AKÇA

IN PARTIAL FULFILLMENT OF THE REQUIREMENTS
FOR
THE DEGREE OF MASTER OF SCIENCE
IN
MECHANICAL ENGINEERING

SEPTEMBER 2024

Approval of the thesis:

IMPLEMENTATION, ASSESSMENT, AND EXTENSION OF THE WRAY-AGARWAL TURBULENCE MODEL FOR SHOCK WAVE-BOUNDARY LAYER INTERACTIONS

submitted by **SEMİH CAN AKÇA** in partial fulfillment of the requirements for the degree of **Master of Science in Mechanical Engineering Department, Middle East Technical University** by,

Prof. Dr. Naci Emre Altun
Dean, Graduate School of **Natural and Applied Sciences** _____

Prof. Dr. Serkan Dağ
Head of Department, **Mechanical Engineering** _____

Assoc. Prof. Dr. Özgür Uğraş Baran
Supervisor, **Mechanical Engineering, METU** _____

Dr. Erdem Dikbaş
Co-supervisor, **Roketsan Inc.** _____

Examining Committee Members:

Prof. Dr. Cüneyt Sert
Mechanical Engineering, METU _____

Assoc. Prof. Dr. Özgür Uğraş Baran
Mechanical Engineering, METU _____

Prof. Dr. Mehmet Metin Yavuz
Mechanical Engineering, METU _____

Assist. Prof. Dr. Onur Baş
Mechanical Engineering, TED University _____

Prof. Dr. Oğuz Uzol
Aerospace Engineering, METU _____

Date: 04.09.2024

I hereby declare that all information in this document has been obtained and presented in accordance with academic rules and ethical conduct. I also declare that, as required by these rules and conduct, I have fully cited and referenced all material and results that are not original to this work.

Name, Surname: Semih Can Akça

Signature :

ABSTRACT

IMPLEMENTATION, ASSESSMENT, AND EXTENSION OF THE WRAY-AGARWAL TURBULENCE MODEL FOR SHOCK WAVE-BOUNDARY LAYER INTERACTIONS

Akça, Semih Can
M.S., Department of Mechanical Engineering
Supervisor: Assoc. Prof. Dr. Özgür Uğraş Baran
Co-Supervisor: Dr. Erdem Dikbaş

September 2024, 71 pages

The use of linear eddy viscosity-based Reynolds-averaged Navier-Stokes (RANS) turbulence modeling is the industry-standard approach rather than directly solving turbulent scales. Thus, accurate turbulence modeling preserves its significance in aerospace problems, especially in high-speed flows involving shock wave-boundary layer interactions (SWBLIs). One-equation turbulence models are commonly used tools due to their lower computational cost compared to two- or more-equation models. The newly derived Wray-Agarwal (WA) turbulence model, a one-equation model based on linear eddy viscosity, is promising as it has demonstrated superiority over the commonly used Spalart-Allmaras model in wall-bounded flows. However, there is a lack of research on the performance of the Wray-Agarwal model in high-speed flows involving SWBLIs. In this thesis, two main versions of the WA model are implemented and verified using an open-source CFD solver. The models are investigated using different SWBLI test cases. Although the WA model shows inadequate performance in heat flux predictions, good agreement between validation results and the experiments is observed in terms of pressure and shear stress predictions for weak

shock-induced separation problems. Two different improvement methodologies from the literature are applied to the Wray-Agarwal model. Consequently, a new formulation is proposed to improve the prediction capabilities of the Wray-Agarwal model for strong shock-induced separations. The modified WA model is found to perform better in compression ramp-type flow problems.

Keywords: Turbulence Modeling, Shock Wave-Boundary Layer Interactions, CFD

ÖZ

WRAY-AGARWAL TÜRBÜLANS MODELİNİN ŞOK DALGASI-SINIR TABAKA ETKİLEŞİMİ KAPSAMINDA UYGULANMASI, DEĞERLENDİRİLMESİ VE GENİŞLETİLMESİ

Akça, Semih Can
Yüksek Lisans, Makina Mühendisliği Bölümü
Tez Yöneticisi: Doç. Dr. Özgür Uğraş Baran
Ortak Tez Yöneticisi: Dr. Erdem Dikbaş

Eylül 2024 , 71 sayfa

Doğrusal çevrinti viskozitesi kullanan Reynolds ortalamalı Navier-Stokes türbülans modellemesi, endüstride türbülans skalalarının doğrudan çözülmesi yerine standart yaklaşım olarak tercih edilmektedir. Bu nedenle türbülans modellerinin isabeti, şok dalgası-sınır tabaka etkileşimli yüksek hızlı akışlar başta olmak üzere, havacılık ve uzay problemlerinde önemini korumaktadır. Tek denklemli türbülans modelleri, iki veya daha fazla denklemli modellere kıyasla daha az hesaplama gücü gerektirdiği için yaygın olarak tercih edilmektedir. Wray-Agarwal türbülans modeli, yeni geliştirilmiş, tek denklemli ve doğrusal çevrinti viskozitesi kullanan bir modeldir. Endüstride yaygın olarak kullanılan Spalart-Allmaras modeline kıyasla duvar ile çevrelenmiş akışlarda üstünlük gösteren Wray-Agarwal modelinin gelecek vaat eden bir model olduğu değerlendirilmektedir. Fakat bu modelin şok dalgası-sınır tabaka etkileşimli, yüksek hızlı sıkıştırılabilir akışlardaki performansına ilişkin literatürde araştırma eksikliği bulunmaktadır. Bu tezde WA modelinin iki farklı ana versiyonu, açık kaynaklı bir HAD çözücüsüne eklenmiş ve modeller doğrulanmıştır. Modeller, çeşitli

şok dalgası-sınır tabaka etkileşimli akış içeren denektaşları kullanılarak incelenmiştir. WA modelinin ısı akısı tahminlerinde yetersiz performans sergilemesine rağmen, zayıf şok kaynaklı ayrılma problemlerinde basınç ve kesme gerilmesi tahminleri için deney verileriyle uyumlu sonuçlar verdiği gözlemlenmiştir. Literatürden seçilmiş iki farklı uyarlama yöntemi model başarımını geliştirme amacıyla Wray-Agarwal modeline uygulanmıştır. Sonuç olarak, şok dalgası kaynaklı kuvvetli akış ayrılmaları için akış tahmin kabiliyetini geliştirmek amacıyla yeni bir model formülasyonu önerilmiştir. Uyarlanmış WA modelinin sıkıştırma rampası tipi akış problemlerinde daha iyi performans gösterdiği tespit edilmiştir.

Anahtar Kelimeler: Türbülans Modelleme, Şok Dalgası-Sınır Tabaka Etkileşimleri, HAD

To my family

ACKNOWLEDGMENTS

I would like to express my deepest gratitude to my supervisors, Assoc. Prof. Dr. Özgür Uğraş Baran and Dr. Erdem Dikbaş, for their guidance, invaluable feedback, and constructive criticism throughout this thesis. They significantly contributed to this study and my understanding of engineering.

I would like to thank the Roketsan Aerodynamics and Engineering Analysis Department family, especially Bilal Okumuş, for their help and for sharing their knowledge and experience. I am also very thankful to my colleague, Ulaş Canberk Ayan, for his insightful discussions and helpful feedback.

Special thanks to my dear friends Erol Furkan Güven and Muhammed Enes Karagöz for their valuable friendship.

Last but of course not least, I am extremely grateful to my father, Abdullah Akça, my mother, Rukiye Akça, and my sisters, Nuran and Dilara, for their endless love, for encouraging me to be a better person, and for everything they have done for me. Being with them makes me feel incredibly fortunate. I could not have written this thesis without their love and support.

TABLE OF CONTENTS

LIST OF TABLES

TABLES

LIST OF FIGURES

FIGURES

LIST OF ABBREVIATIONS

ABBREVIATONS	
2D	Two Dimensional
3D	Three Dimensional
BC	Boundary Condition
CFD	Computational Fluid Dynamics
CFL	Courant-Friedrichs-Lewy Condition
CFL3D	Computational Fluids Laboratory Three-Dimensional
DNS	Direct Numerical Simulations
EARSM	Explicit Algebraic Reynolds Stress Model
FUN3D	Fully Unstructured Navier-Stokes Three-Dimensional
HLLC	Harten-Lax-van Leer Contact
NASA TMR	National Aeronautics and Space Administration Turbulence Modeling Resource
RANS	Reynolds-Averaged Navier-Stokes
SA	Spalart-Allmaras
SU	Shock Unsteadiness
SUQ-SST	K-Omega SST Shock Unsteadiness
SWBLI	Shock Wave-Boundary Layer Interaction
WA	Wray-Agarwal
WA2017	Wray-Agarwal 2017
WA2018	Wray-Agarwal 2018
WA2018S-1	Wray-Agarwal 2018 Anisotropy-1
WA2018S-2	Wray-Agarwal 2018 Anisotropy-2
WA2018SU	Wray-Agarwal 2018 Shock Unsteadiness

LIST OF SYMBOLS

SYMBOLS

$C_1^{'}$	Modified Production Term Coefficient of Wray-Agarwal Turbulence Model
ρ	Density
C_{μ}^{*}	Anisotropy Parameter
δ_0	Boundary Layer Thickness
D	Deformation Rate Tensor Magnitude
ε	Turbulence Dissipation Rate
Q_{∞}	Free Stream Heat Flux
P_{∞}	Free Stream Pressure
Q	Heat Flux
k	Turbulent Kinetic Energy
M	Mach Number
$F_1^{'}$, $F_2^{'}$	Modified Blending Function
$a_1^{'}$	Modified Structure Parameter
S_{ii}	Normal Strain
ω	Specific Turbulence Dissipation Rate
C_p	Pressure Coefficient
P	Pressure
Re	Reynolds Number
f_s	Shock Detection Function
β	Shock Generator Angle
C_f	Skin-Friction Coefficient
c_1	Upstream Speed of Sound
S	Strain Rate Magnitude
$a_1^{''}$	Structure Parameter Limiter
a_1	Structure Parameter

c_{b1}	Modified Production Term Coefficient of Spalart-Allmaras Turbulence Model
$b_1^{'}$, $c_{\varepsilon 1}$	Shock Unsteadiness Model Coefficients
T	Temperature
t	Time
P_0	Total Pressure
T_0	Total Temperature
τ	Turbulence Time Scale
μ_T	Turbulent Viscosity
M_{1n}	Upstream Mach Number Normal with respect to Shock Wave
W, Ω	Vorticity Magnitude
f_1, F_2	Blending Function
C_1, $C_{k\varepsilon}$, $C_{k\omega}$	Wray-Agarwal Turbulence Model Coefficients
f_μ	Damping Function
d	Wall Distance
Q_w	Wall Heat Flux
P_w	Wall Pressure
T_w	Wall Temperature

CHAPTER 1

INTRODUCTION

Computational Fluid Dynamics (CFD) has been an essential tool for engineering design and analysis processes since the 1960s. The usage of CFD has increased over time thanks to advancements in computing power. The accuracy of this method has grown in line with this rise in usage as more physics is introduced into the numerical solutions. The dynamics of fluid flows are governed by the well-known Navier-Stokes equations. Although analytical or direct numerical solutions of the Navier-Stokes equations for simple flows with low Reynolds numbers exist, their application for turbulent flows with high Reynolds numbers is not feasible with today's computer capability [1]. Therefore, the employment of Reynolds-averaged Navier-Stokes (RANS) equations with turbulence models is general practice for a wide range of engineering flow problems.

The RANS methodology involves splitting the instantaneous quantities into portions that represent averages and fluctuations. However, this procedure leads to a closure problem since it introduces additional unknowns to the system of PDEs. To close the equation set, a turbulence model is required for the depiction of the Reynolds stresses, which are the product of the Reynolds decomposition process. Numerous studies on turbulence modeling have been conducted; either new models have been developed, or existing ones have been modified [2]. Despite the availability of many different formulations for turbulence modeling, engineers and scientists have predominantly utilized three models for numerical simulations of compressible aerodynamics: the $k-\omega$ SST, $k-\varepsilon$ Realizable, and Spalart-Allmaras model.

As a matter of fact, no one- or two-equation turbulence model consistently provides good predictions for different types of fluid flows. Thus, there has been a contin-

uous endeavor to improve engineering flow predictions using RANS models. The recently derived Wray-Agarwal turbulence model is a good example of this effort. The Wray-Agarwal (WA) model is a one-equation, eddy viscosity-based turbulence model developed by T. J. Wray and R. K. Agarwal [3]. The model equation is derived from Wilcox's $k-\omega$ model [4] closure. Unlike previous $k-\omega$ closure-based one-equation models such as the model by Fares et al. [5], the cross-diffusion term from the ω equation is retained in the derivation of the WA model. Therefore, it differs from other $k-\omega$ closure-based one-equation models. Also, the WA model behaves similarly to the $k-\varepsilon$ model in the far-field regions, and it carries the characteristics of the $k-\omega$ model closer to the wall. Consequently, the advantages of these two-equation models are combined into a one-equation model.

Even though the Spalart-Allmaras (SA) and two-equation models are more frequently preferred compared to the WA model by the CFD community for the analyses of fluid flows, prior research [3, 6, 7] indicates that the WA model is superior to the SA model for wall-bounded flows and is competitive with two-equation models. For this reason, we considered that the WA model has the potential to be preferred for routine aerodynamic simulations due to its lower computational cost, ease of implementation aspect, and competitive performance compared to the commonly used two-equation turbulence models. However, research performed by Acquaye et al. [8] shows that the WA turbulence model falls short in the prediction of shock wave-boundary layer interaction (SWBLI) flows. Also, there is a certain lack of research on the performance and assessment of the WA model in the context of SWBLIs. Therefore, improving the prediction capabilities of the WA model following an extensive validation and assessment study could be valuable research, which is the primary motivation of this thesis.

1.1 Background

Shock wave-boundary layer interactions (SWBLIs) are observed in various engineering applications involving high-speed flows, e.g., supersonic flight, intakes of air-breathing missiles, and aircraft. These interactions are significant as they cause flow unsteadiness, aeroelastic buffeting, and various other potential effects that can lead to

impairment [9]. Despite its vitalness, accurate simulation of the interaction between turbulent boundary layers and shock waves remains challenging.

Solving high-speed engineering flows with RANS modeling is the standard approach as opposed to directly solving turbulent scales. This situation seems to remain so in the following years due to the size of the industrial-scale problems and the level of computer technology. Many efforts have been made to enhance the prediction capabilities of turbulence models in the context of SWBLI flows [10].

A good example of these improvement attempts is the shock unsteadiness modification by Sinha et al. [11]. Across the shock wave, the eddy viscosity-based RANS models predict high amplification of the turbulent kinetic energy, k, which can be seen in Figure 1.1. The shock is located at nearly $x = 2$, where turbulent kinetic energy shows a sudden increase followed by a sudden decrease. Standard eddy viscosity models do not capture this sudden decrease followed by the increase. To solve this inconsistency, the turbulent kinetic energy was tried to be suppressed in several studies, such as Realizability modification by Thivet et al. [12]. The suppression of the turbulent kinetic energy amplification with different techniques resulted in improved accuracy. However, Sinha et al. [11] showed that the performance of these suppression techniques deteriorates as the Mach number increases (Figure 1.2).

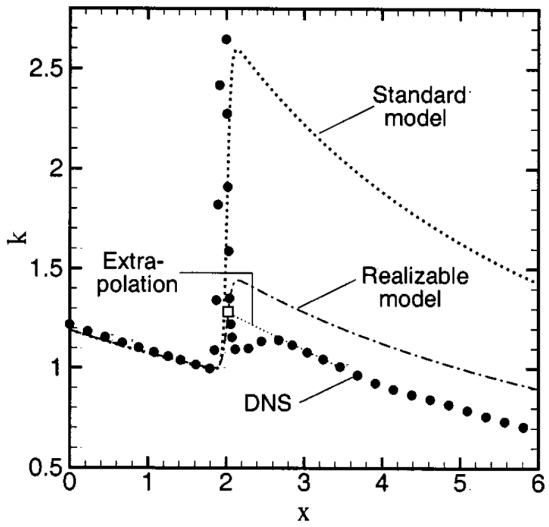

Figure 1.1: Turbulent kinetic energy k related to different $k - \varepsilon$ models in the homogeneous turbulence with Mach 1.29 normal shock. Retrieved from [11]

Sinha et al. [11] introduced the effect of shock unsteadiness on the turbulent kinetic energy equation of the $k - \varepsilon$ model using linear analysis for isotropic turbulence. Moreover, they modified the amplification of the dissipation rate equation. Their model improved the performance of the $k - \varepsilon$ model in terms of turbulent kinetic energy, as shown in Figure 1.2. More details about Sinha's shock unsteadiness study are given in Section 2.2.1.

Sinha's work is not the only research aiming to improve turbulence models for fluid flow simulations with SWBLIs. There have been many attempts to enhance the performance of Menter's $k - \omega$ SST model. Menter's $k - \omega$ SST model [13] is one of the most preferred turbulence models amongst equation-based models, and it is frequently utilized for external and internal aerodynamic flows. Even though the $k - \omega$ SST model performs exceptionally well in low-speed flows [14], it produces erratic results in high-speed shock-induced separated flows [15]. Therefore, further research efforts have been conducted to enhance the precision of the $k - \omega$ SST model within the context of SWBLI flows, e.g., the application of Bayesian parameter estimation by Tang et al. [16] and stress limiter consideration by Tan et al. [17]. A common research topic to increase the accuracy of the $k-\omega$ SST model is modifying the structure parameter (a.k.a. proportionality constant), a_1, appearing in the eddy viscosity estimation. Improvements have been obtained despite the fact that the majority of these alterations are implemented by trial and error [18]. However, these improvements are case-dependent since the modifications are tailored for specific cases.

A more systematic approach was adopted by Raje and Sinha, who introduced improvements to the $k - \omega$ SST model to enhance the SWBLI prediction capabilities with a model named SUQ-SST [19]. They modified the structure parameter to have a better agreement with experimental data such that the structure parameter becomes a function of the local velocity gradients. Also, they introduced Reynolds stress anisotropy in the definition of turbulent viscosity to better capture the physics. They adopted a formulation based on Rung et al.'s Explicit Algebraic Reynolds Stress Model (EARSM) [20] amongst several alternatives. A notable outcome of this study was that the overall accuracy of SWBLI predictions was improved when the anisotropy was incorporated into the eddy viscosity definition of $k-\omega$ SST model. More details about Raje and Sinha's anisotropic $k - \omega$ SST study are given in Section 2.2.2.

Various research efforts in the literature aim to enhance the behavior of the WA turbulence model. However, the majority of these studies have concentrated on subsonic flows [7, 21, 22, 23]. The high-speed flow performance of the WA model was briefly validated by Acquaye et al. [8], but no efforts were made to improve it in the context of SWBLI flows. Therefore, we considered that applying similar modification techniques described in this section to the WA model would be a valuable area of study.

1.2 Objectives and Outline of the Thesis

The first objective of this thesis is to perform a comprehensive study to assess the prediction capabilities and performance of the WA model in SWBLI flows. For this purpose, we have implemented the WA model into an open-source flow solver. To assess the models in SWBLI flows, four different test cases with different interaction types and Mach regimes were selected. Moreover, the WA model is compared to the Spalart-Allmaras model in the context of SWBLI flows.

The second objective is to enhance the WA model performance in the SWBLI flows by utilizing different techniques from the literature so that the deficiencies of the WA model are eliminated. Therefore, CFD practitioners would be able to utilize the WA model in different flow types and regimes without sacrificing accuracy in high-speed flows.

This thesis has five chapters, including the introduction given until here. The other chapters are summarized as follows:

- Chapter 2 gives the theory behind the work done in this thesis. This chapter includes the theory of the WA models, existing attempts to improve the turbulence models for SWBLI flows and an open-source CFD solver utilized in this thesis.

- Chapter 3 exhibits the results, which consist of the implementation and verification of the Wray-Agarwal model, the validation and assessment study with explanations of the test cases, and their results with the standard WA model.

- Chapter 4 consists of two sections: the theory of current modification attempts on the Wray-Agarwal 2018 (WA2018) model and their results with the same test cases used in the validation study in Chapter 3.
- Finally, Chapter 5 concludes the thesis and makes future work recommendations.

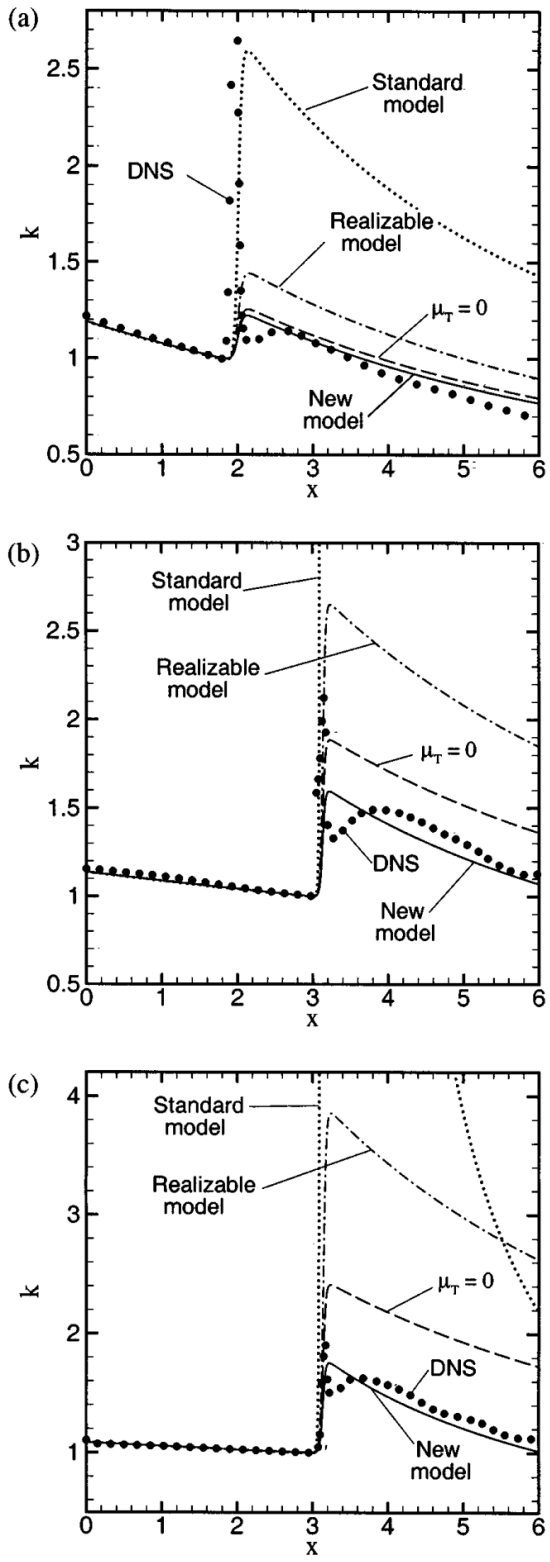

Figure 1.2: Turbulent kinetic energy, k, related to different $k - \varepsilon$ models and Sinha et al.'s model in the homogeneous turbulence with a normal shock at Mach: (a) 1.29, (b) 2.0, and (c) 3.0. Retreived from [11]

CHAPTER 2

THEORY

This chapter is composed of three sections describing the standard Wray-Agarwal turbulence models, existing SWBLI improvement methodologies, and an open-source CFD flow solver used in this thesis.

2.1 Wray-Agarwal Turbulence Models

The derivation and details of the Wray-Agarwal turbulence model are given in the original paper published in 2015 [3]. The WA model is derived from Wilcox's $k-\omega$ closure by defining the model's transport parameter as $R = k/\omega$, where k is turbulent kinetic energy, and ω is specific dissipation rate. By substituting the k and ω equations in Eqs. (2.1) and (2.2) into the material derivative of R in Eq. (2.3), the WA model is obtained where Bradshaw's relation given in Eq. (2.4) is used to complete the closure. These substitution processes end up with the transport equation of the WA model given in Eq. (2.5).

$$\frac{Dk}{Dt} = \frac{\partial}{\partial y}\left(\sigma_k \frac{k}{\omega}\frac{\partial k}{\partial y}\right) + \nu_t \left(\frac{\partial u}{\partial y}\right)^2 - \beta^* k\omega \tag{2.1}$$

$$\frac{D\omega}{Dt} = \frac{\partial}{\partial y}\left(\sigma_\omega \frac{k}{\omega}\frac{\partial \omega}{\partial y}\right) + \alpha\frac{\omega}{k}\nu_t \left(\frac{\partial u}{\partial y}\right)^2 - \beta\omega^2 + \frac{\sigma_d}{\omega}\frac{\partial k}{\partial y}\frac{\partial \omega}{\partial y} \tag{2.2}$$

$$\frac{DR}{Dt} = \frac{1}{\omega}\frac{Dk}{Dt} - \frac{k}{\omega^2}\frac{D\omega}{Dt} \tag{2.3}$$

$$\left|-\overline{u'v'}\right| = \nu_t \left|\frac{\partial u}{\partial y}\right| = a_1 k \tag{2.4}$$

$$\frac{DR}{Dt} = \frac{\partial}{\partial y}\left(\sigma_R R \frac{\partial R}{\partial y}\right) + C_1 R \left|\frac{\partial u}{\partial y}\right| + C_2 \frac{R}{\left|\frac{\partial u}{\partial y}\right|}\frac{\partial R}{\partial y}\frac{\partial \left|\frac{\partial u}{\partial y}\right|}{\partial y} - C_3 R^2 \left(\frac{\frac{\partial \left|\frac{\partial u}{\partial y}\right|}{\partial y}\frac{\partial \left|\frac{\partial u}{\partial y}\right|}{\partial y}}{\left|\frac{\partial u}{\partial y}\right|^2}\right) \tag{2.5}$$

After several modifications, different versions of the WA model were proposed in 2017 and 2018 [6, 7]. Both versions are listed as standard models by the NASA Turbulence Modeling Resource (TMR) website [24]. Both 2017 and 2018 formulations of the Wray-Agarwal turbulence model have been implemented into the CFD solver $flowPsi$, within the scope of the current thesis study. This section describes the details of these models.

2.1.1 Wray-Agarwal 2017 Model

The partial differential equation with regard to the Wray-Agarwal 2017 (WA2017) model by T. J. Wray and R. K. Agarwal [6] is given by Eq. (2.6).

$$\frac{\partial R}{\partial t} + \frac{\partial u_j R}{\partial x_j} = \frac{\partial}{\partial x_j}\left[\left(\sigma_R R + \nu\right)\frac{\partial R}{\partial x_j}\right] + C_1 R S + f_1 C_{2k\omega}\frac{R}{S}\frac{\partial R}{\partial x_j}\frac{\partial S}{\partial x_j} - \left(1 - f_1\right) C_{2k\epsilon} R^2 \left(\frac{\left(\frac{\partial S}{\partial x_j}\frac{\partial S}{\partial x_j}\right)}{S^2}\right) \tag{2.6}$$

The first version of the WA2017 model shows non-physical behaviors in zero-strain regions because of the destruction term of Eq. (2.6). Han et al. [7] proposed a bound in the formulation, which is given by Eq. (2.7). Some of the model constants were also updated. We adopt the newer version of the WA2017 model given in Eq. (2.7) in this study.

$$\frac{\partial R}{\partial t} + \frac{\partial u_j R}{\partial x_j} = \frac{\partial}{\partial x_j}\left[(\sigma_R R + \nu)\frac{\partial R}{\partial x_j}\right] + C_1 RS + f_1 C_{2k\omega}\frac{R}{S}\frac{\partial R}{\partial x_j}\frac{\partial S}{\partial x_j} - (1-f_1)min\left[C_{2k\epsilon}R^2\left(\frac{\frac{\partial S}{\partial x_j}\frac{\partial S}{\partial x_j}}{S^2}\right), C_m\frac{\partial R}{\partial x_j}\frac{\partial R}{\partial x_j}\right] \quad (2.7)$$

The solution of R-transport-equation affects the governing equations of the flow through the local quantity of turbulent viscosity. The turbulent viscosity is approximated using the relation given by Eq. (2.8), and f_μ stands for the damping function, which is given by Eq. (2.9).

$$\nu_T = f_\mu R \quad (2.8)$$

$$f_\mu = \frac{\chi^3}{\chi^3 + C_\omega^3},\ \chi = \frac{R}{\nu} \quad (2.9)$$

The transport equation acts as a one-equation model based on the standard $k-\omega$ closure when the $C_{2k\omega}$ term dominates. Similarly, the behavior shifts towards the standard $k-\varepsilon$ closure when the $C_{2k\varepsilon}$ term is active. The $C_{2k\varepsilon}$ term is a product of the inclusion of cross-diffusion in the derivation process from $k-\omega$ closure, which differs the WA model from the other $k-\omega$ based one equation models such as Fares and Schröder's model [5]. The behavioral change is controlled by the blending function, f_1, which is given in Eq. (2.10). The maximum limiting value of 0.9 in the definition of f_1 is set for better stability characteristics. Also, a formula is constructed for arg_1 given in Eq. (2.11), where d is the wall distance. The distance to the nearest wall for each cell is used to compute the wall distance.

$$f_1 = min(tanh(arg_1^4), 0.9) \quad (2.10)$$

$$arg_1 = \frac{1 + \frac{d\sqrt{RS}}{\nu}}{1 + \left[\frac{max\left(d\sqrt{RS}, 1.5R\right)}{20\nu}\right]^2} \quad (2.11)$$

The blending function, f_1, is a bounded and smooth hyperbolic function, which is formulated such that $C_{2k\omega}$ dominates in the viscous sublayer and the majority of the log-layer, and $C_{2k\varepsilon}$ dominates near the outer boundary of the log-layer.

The constants of the WA2017 model are given in Eq. (2.12).

$$\begin{gathered} C_{1k\omega} = 0.0829,\ C_{1k\varepsilon} = 0.1127 \\ C_1 = f_1\left(C_{1k\omega} - C_{1k\varepsilon}\right) + C_{1k\varepsilon} \\ \sigma_{k\omega} = 0.72,\ \sigma_{k\varepsilon} = 1.0 \\ \sigma_R = f_1\left(\sigma_{k\omega} - \sigma_{k\varepsilon}\right) + \sigma_{k\varepsilon} \\ \kappa = 0.41,\ C_w = 8.54,\ C_m = 8.0 \\ C_{2k\omega} = \frac{C_{1k\omega}}{\kappa^2} + \sigma_{k\omega},\ C_{2k\varepsilon} = \frac{C_{1k\varepsilon}}{\kappa^2} + \sigma_{k\varepsilon} \end{gathered} \tag{2.12}$$

2.1.2 Wray-Agarwal 2018 Model

The dependency on the wall distance, d, of Eq. (2.11) can result in inaccuracies and higher computing costs. The WA2018 model, a wall distance-free alternative, was proposed as a remedy to these drawbacks. The model equation in Eq. (2.7) was kept the same for this version. On the other hand, the arg_1 was modified such that it does not depend on wall distance, which is given in Eq. (2.14). This was performed by introducing auxiliary relations in Eq. (2.15).

$$f_1 = tanh(arg_1^4) \tag{2.13}$$

$$arg_1 = \frac{\nu + R}{2}\frac{\eta^2}{C_\mu k\omega} \tag{2.14}$$

$$\begin{gathered} k = \frac{\nu_T S}{\sqrt{C_\mu}},\ \omega = \frac{S}{\sqrt{C_\mu}} \\ \eta = S\, max\left(1, \left|\frac{W}{S}\right|\right) \\ W = \sqrt{2W_{ij}W_{ij}},\ W_{ij} = \frac{1}{2}\left(\frac{\partial u_i}{\partial x_j} - \frac{\partial u_j}{\partial x_i}\right) \end{gathered} \tag{2.15}$$

Also, the constants given in Eq. (2.16) were updated. The remaining constants were kept the same as in the previous version.

$$\begin{aligned} C_{1k\varepsilon} &= 0.1284 \\ C_{\mu} &= 0.09 \end{aligned} \tag{2.16}$$

2.2 Existing Model Improvements for SWBLI Flows

Two existing shock improvement methodologies from the literature are presented in this section. We chose these two methodologies given in Sections 2.2.1 and 2.2.2 since they are the most systematic approaches to enhance turbulence model behaviors compared to others in the literature for SWBLI flows. The selected methodologies are applied to the WA model in Chapter 4.

2.2.1 Shock Unsteadiness Model

According to Sinha et al. [11], the turbulent kinetic energy across the shock is excessively amplified by eddy viscosity-based RANS models. Therefore, they came up with modified turbulent kinetic energy and dissipation rate equations based on linear analysis results. This modification substantially improves the $k-\varepsilon$ model's performance. The details of this work can be found in [11] and in Section 1.1.

Sinha applied the modifications mentioned in Section 1.1 to the Spalart-Allmaras model in a research [25]. In this study, it was stated that the amplification of turbulent kinetic energy was driven by the production term in the SA transport equation. This study showed that the addition of Eq. (2.18) to the production term of the model improves the prediction characteristics of the Spalart-Allmaras model in SWBLI flows.

$$\frac{k_2}{k_1} = \left(\frac{\tilde{u}_{n,1}}{\tilde{u}_{n,2}}\right)^{\frac{2}{2}\left(1-b_1'\right)} \; and \; \frac{\varepsilon_2}{\varepsilon_1} = \left(\frac{\tilde{u}_{n,1}}{\tilde{u}_{n,2}}\right)^{\frac{2}{2}c_{\varepsilon 1}} \tag{2.17}$$

$$
\begin{aligned}
b_1^{'} &= 0.4\left[1 - exp\left(1 - M_{1n}\right)\right] \\
c_{\varepsilon 1} &= 1.25 + 0.2\left(M_{1n} - 1\right)
\end{aligned}
\tag{2.18}
$$

In Eq. (2.18), the subscript '1' denotes upstream of the shock wave while '2' denotes downstream . The M_{1n} indicates the normal component of the upstream Mach number with respect to the shock wave. The M_{1n} is calculated via the dot product of vectorized upstream Mach and pressure gradient vector, as given in Eq. (2.19).

$$
M_{1n} = \frac{\mathbf{u}_1}{c_1} \cdot \frac{\nabla P}{|\nabla P|} \tag{2.19}
$$

The eddy viscosity definition of the Spalart-Allmaras model is proportional to k^2/ε. Also, the change in turbulent viscosity across a shock wave was estimated as in Eq. (2.20) by Sinha [25]. Thus, the substitution of Eq. (2.17) into Eq. (2.20) gives Eq. (2.21). By equating powers of both sides in Eq. (2.21), the relation in Eq. (2.22) is obtained.

$$
\frac{\tilde{\nu}_2}{\tilde{\nu}_1} = \left(\frac{k_2}{k_1}\right)^2 \frac{\varepsilon_1}{\varepsilon_2} = \left(\frac{\tilde{u}_{n,1}}{\tilde{u}_{n,2}}\right)^{c_{b1}^{'}} \tag{2.20}
$$

$$
\frac{\tilde{\nu}_2}{\tilde{\nu}_1} = \left(\left(\frac{\tilde{u}_{n,1}}{\tilde{u}_{n,2}}\right)^{\frac{2}{2}\left(1-b_1^{'}\right)}\right)^2 \left(\left(\frac{\tilde{u}_{n,1}}{\tilde{u}_{n,2}}\right)^{\frac{2}{2}c_{\varepsilon 1}}\right)^{-1} = \left(\frac{\tilde{u}_{n,1}}{\tilde{u}_{n,2}}\right)^{c_{b1}^{'}} \tag{2.21}
$$

$$
c_{b1}^{'} = \frac{4}{3}\left(1 - b_1^{'}\right) - \frac{2}{3}c_{\varepsilon 1} \tag{2.22}
$$

Eq. (2.22) is used in the production term of the Spalart-Allmaras model instead of c_{b1}. It is also mentioned by Sinha [25] that this modification is only applied in regions of high dilation. Thus, the standard behavior of the Spalart-Allmaras model is kept the same elsewhere.

2.2.2 Reynolds Anisotropy Inclusion

It is shown by Georgiadis et al. [18] that changing the value of constant structure parameter, a_1, of the $k-\omega$ SST model's turbulent viscosity formulation given in Eq. (2.23) has led to improved predictions on SWBLI flows.

$$\mu_T = \frac{\bar{\rho} a_1 k}{max\left(a_1\omega, \Omega F_2\right)} \tag{2.23}$$

By modifying the structure parameter as well as the eddy viscosity definition, Raje and Sinha [19] obtained better accuracy for SWBLIs. In that study, they suggested that the a_1 could be calculated through the mean velocity field by utilizing EARSM approximations. For this purpose, the EARSM of Rung et al. [20] is utilized to introduce turbulence anisotropy. The details of Rung et al.'s EARSM are given in Eqs. (2.24), (2.25) and (2.26).

$$\mu_T = \frac{C_\mu^*}{C_\mu}\frac{\bar{\rho}k}{\omega} \tag{2.24}$$

$$C_\mu^* = \frac{\beta_1^{'}}{1-\frac{2}{3}\eta^2+2\xi^2} \tag{2.25}$$

$$\beta_1^{'} = \tfrac{\frac{4}{3}-C_2}{2g},\ \beta_2^{'} = \tfrac{2-C_4}{2g},\ \beta_3^{'} = \tfrac{2-C_3}{g}$$

$$\eta^2 = \tfrac{\beta_3^{'2}\hat{S}^2}{8},\ \xi^2 = \tfrac{\beta_2^{'2}\hat{\Omega}^2}{2},\ g = g_{ic} + g_c$$

$$g_{ic} = f_g\left(C_1 - 1\right) + \psi,\ f_g = 1 + 0.95\left(1 - tanh\left(\tfrac{\hat{S}^2}{4.6225}\right)\right) \tag{2.26}$$

$$\psi = \tfrac{\hat{S}^2}{4+1.83\sqrt{0.8\hat{\Omega}^2+0.2\hat{S}^2}}$$

$$g_c = 0.15M_t\left[\tfrac{P}{\bar{\rho}\epsilon} - \tfrac{4}{3}M_t\right],\ \tfrac{P}{\bar{\rho}\epsilon} = \tfrac{0.8+\psi}{1.9}$$

The anisotropy parameter, C_μ^*, is approximated by the relations in Eqs. (2.25) and (2.26). The non-dimensional vorticity magnitude and strain-rate magnitude are de-

fined as $\hat{\Omega} = \tau\Omega$, $\hat{S} = \tau S$ where the turbulence time scale is $\tau = 1/\left(C_\mu \omega\right)$. Utilizing Sarkar's pressure-dilatation model, compressibility correction, g_c, is implemented. Also, the turbulent Mach number is defined as $M_t = \sqrt{2k}/\tilde{a}$, where $\tilde{a}$ is the Favre-averaged speed of sound. Constants and other details of the model can be found in [19].

Using the EARSM of Rung et al., Raje and Sinha proposed an alternative structure parameter. The modified structure parameter based on the anisotropy parameter, C_μ^*, is given by Eq. (2.27).

$$a_1^{'} = C_\mu^* \tau D \left[1 - \tau D \left(\beta_2^{'} - \beta_3^{'}\right)\right] \tag{2.27}$$

In Eq. (2.27), D stands for the magnitude of the deformation rate tensor, which includes both strain rate and vorticity. For this reason, unphysically high values can be observed from $a_1^{'}$, especially close to shock locations. Therefore, the use of limiters is necessary. In this regard, the shock unsteadiness (SU) model [11] introduction to the SUQ-SST model is considered to be useful for near-shock wave calculations. However, the dependency on the upstream Mach number of the SU model complicates the implementation. Therefore, Raje and Sinha selected a limiter $a_1^{''} = 0.4$, based on experiments [19]. Therefore, the modified eddy viscosity is defined as given in Eq. (2.29).

$$\mu_T = \frac{\bar{\rho} a_1^{''} k}{D} \tag{2.28}$$

After determining the structure parameter, the eddy viscosity definition can be combined for $a_1^{'}$ and $a_1^{''}$, as shown in Eq. (2.29). Eddy viscosity definition in Eq. (2.29) will likely produce floating-point exceptions due to possible vanishing denominator occurrences.

$$\begin{aligned} \mu_T &= \frac{\bar{\rho} a_1^* k}{D} = \frac{\bar{\rho} a_1 k}{D\left(a_1/a_1^*\right)} \\ a_1^* &= min\left[a_1^{'}, a_1^{''}\right] \end{aligned} \tag{2.29}$$

Raje and Sinha suggested a solution for this runtime problem by coupling Eq. (2.29)

with the eddy viscosity expression in Eq. (2.24). Finally, the eddy viscosity definition of Raje and Sinha's SUQ-SST becomes as in Eq. (2.30).

$$\mu_T = \frac{\bar{\rho} a_1 k}{max\left[\left(1 - F_2^{'}\right)\left(\frac{C_\mu}{C_\mu^*}\right) a_1 \omega, F_2^{'} D\left(\frac{a_1}{a_1^*}\right)\right]} \tag{2.30}$$

$$\begin{gathered} F_2^{'} = max\left[F_2, f_s\right] \\ f_s = \tfrac{1}{2} - \tfrac{1}{2} tanh\left(arg\right) \\ arg = 50\tfrac{S_{ij}}{\tau_s} + 5,\ \tau_s = \tfrac{\tilde{a}}{L_S} \\ L_S = max\left(\Delta, L_\epsilon\right),\ L_\epsilon = \tfrac{0.25\sqrt{k}}{0.09\omega} \end{gathered} \tag{2.31}$$

In Eq. (2.31), F_2 and f_s are used to build the blending function $F_2^{'}$, where F_2 detects turbulent boundary layers and f_s detects shock waves.

2.3 CFD Solver: $flowPsi$

In this thesis, we implemented the WA models and our contributions to the open-source flow solver $flowPsi$, developed by Luke et al. [26]. $FlowPsi$ solves steady or unsteady flow problems of the Euler and Navier-Stokes equations with unstructured-type grids. It is a Finite Volume-based, unstructured, compressible flow solver built on an infrastructure called Loci [27]. $FlowPsi$ was developed on the Loci platform, which is a rule-based programming framework and C++ library aimed at the development of computational simulations providing automatic parallelization, finite-volume tools, and other utilities [28].

Our primary motivation of utilizing $flowPsi$ is its rule-based structure, which makes it extremely easy to incorporate new turbulence models as modules. The Wray-Agarwal turbulence models are added to $flowPsi$, which already has a number of turbulence models. All simulations and comparisons are applied with existing and currently implemented models in $flowPsi$. Also, the simulations are performed us-

ing a second-order accurate HLLC flux scheme [29] with the Venkatakrishnan limiter [30] and appropriate CFL numbers for each problem.

The open-source flow solver $flowPsi$ and its turbulence models have been verified in earlier studies [31, 32].

2.3.1 Governing Equations

The finite-volume approach is used to discretize the flow equations. The vector form of governing equations for a 3D flow for an arbitrary control volume Ω_c with a boundary $\partial\Omega_c$ is given in Eq. (2.32) after integration over a computational cell.

$$\frac{d}{dt}\int\limits_{\Omega_c(t)} Q\,dV + \int\limits_{\Omega_c(t)} (F_i - F_v)\,dS = 0 \tag{2.32}$$

The conservative state variables, Q, F_i, and F_v are given in Eq. (2.33).

$$Q = \begin{bmatrix} \rho \\ \rho\tilde{u} \\ \rho e_0 \end{bmatrix},\ F_i = \begin{bmatrix} \rho\tilde{u}\cdot\tilde{n} \\ \left(\rho\tilde{u}\tilde{u} + p\tilde{\tilde{I}}\right)\cdot\tilde{n} \\ (\rho e_0 + p)\,\tilde{u}\cdot\tilde{n} \end{bmatrix},\ F_v = \begin{bmatrix} 0 \\ \tilde{\tilde{\tau}}\cdot\tilde{n} \\ \left(\tilde{u}\cdot\tilde{\tilde{\tau}} + \tilde{q}\right)\cdot\tilde{n} \end{bmatrix} \tag{2.33}$$

The relations in Eqs. (2.34-2.37) are used to close the equation set.

$$p = \rho\tilde{R}T \tag{2.34}$$

$$\tilde{q} = k\nabla T \tag{2.35}$$

$$e_0 = \frac{1}{2}\tilde{u}\cdot\tilde{u} + e_{internal} \tag{2.36}$$

$$e_{internal} = \frac{\tilde{R}T}{\gamma - 1} \tag{2.37}$$

2.3.2 Turbulence Models in $flowPsi$

In $flowPsi$, several turbulence models are available. These models generally include several variations of each model. For example, the $k-\omega$ model family includes the Menter's SST, the Menter's Baseline, Wilcox98, and Wilcox08 $k-\omega$ model formulations. The Spalart-Allmaras model is also available in the $flowPsi$.

The details of the Spalart-Allmaras turbulence model taken from the $flowPsi$ guide [28] are given in Eqs. (2.38), (2.39), and (2.40).

$$\frac{\partial \rho\tilde{\nu}}{\partial t} + \frac{\partial u_j \rho\tilde{\nu}}{\partial x_j} = \rho c_{b1}\tilde{S}\tilde{\nu} - \rho c_{\omega 1} f_\omega \left(\frac{\tilde{\nu}}{y}\right)^2 + \frac{\rho}{\sigma}\frac{\partial}{\partial x_k}\left[(\nu+\tilde{\nu})\frac{\partial \tilde{\nu}}{\partial x_k}\right] + \frac{\rho c_{b2}}{\sigma}\frac{\partial \tilde{\nu}}{\partial x_k}\frac{\partial \tilde{\nu}}{\partial x_k} \tag{2.38}$$

$$\nu_t = \tilde{\nu} f_{v1} \tag{2.39}$$

$$c_{b1} = 0.1355,\ c_{b2} = 0.622,\ c_{v1} = 7.1,\ \sigma = 2/3$$

$$c_{\omega 1} = \frac{c_{b1}}{\kappa^2} + \frac{(1+c_{b2})}{\sigma},\ c_{\omega 2} = 0.3,\ c_{\omega 3} = 2,\ \kappa = 0.41$$

$$f_{v1} = \frac{\chi^3}{\chi^3 + c_{v1}^3},\ f_{v2} = 1 - \frac{\chi}{1+\chi f_{v1}} \tag{2.40}$$

$$f_\omega = g\left[\frac{1+c_{\omega 3}^6}{g^6 + c_{\omega 3}^6}\right]^{1/6},\ \chi = \frac{\tilde{\nu}}{\nu},\ g = r + c_{\omega 2}\left(r^6 - r\right)$$

$$r = \frac{\tilde{\nu}}{\tilde{S}\kappa^2 y^2},\ \tilde{S} = S + \frac{\tilde{\nu}}{\kappa^2 y^2} f_{v2},\ S = \sqrt{2\Omega_{ij}\Omega_{ij}}$$

CHAPTER 3

IMPLEMENTATION AND VALIDATION OF THE WRAY-AGARWAL TURBULENCE MODEL

In this section, the implementation and verification processes of the Wray-Agarwal models are presented. After that, comprehensive validation and assessment studies are given.

3.1 Implementation and Verification of the Wray-Agarwal Model

As mentioned in Section 2.3, we utilized the $flowPsi$ as the CFD solver for model implementations. After the model implementation codes are completed, the results of the standard verification test cases taken from the literature and the $flowPsi$ results are presented in this section.

The verification procedure is necessary to ensure that the implemented codes function properly and that the results are similar to those of the original studies. The flat plate, wall-mounted hump, and backward-facing step problems are selected for verification purposes. These three problems are presented as turbulence model verification and validation problems in the NASA Turbulence Modeling Resource webpage [24]. The data of the original WA models are taken from the study performed by Han et al. [7] for verification of our implementations for both the WA2017 and WA2018 models. After these verification studies, we observed that our implementation of WA model versions into the $flowPsi$ code produces consistent results with the reference CFD results.

The grids used in these verification test case runs are acquired from the NASA TMR

website. The solutions of the verification test cases are available with both CFL3D and FUN3D solvers. The mesh independence studies were performed, and solutions were found to be independent of the grids using CFL3D and FUN3D solvers. Both of these solvers have second-order accurate spatial differencing techniques alongside the implicit time advancement strategy [33]. Since the $flowPsi$ has similar solution methodologies with the same order of accuracy, the same solution grids are used for verification studies without performing mesh independence.

NASA TMR website provides five levels of grid resolutions for each case ranging from coarsest to finest. The second finest grids are used in the following verification simulations.

3.1.1 Flat-Plate

The given description of the 2D zero pressure gradient flat plate verification case in Figure 3.1 is taken from the NASA Turbulence Modeling Resource webpage [24]. Figure 3.2 illustrates that the WA model results from $flowPsi$ demonstrate good agreement with the reference WA skin friction coefficient findings for the flat-plate verification test case.

3.1.2 Wall-Mounted Hump

From the NASA Turbulence Resource webpage [24], the description of the 2D wall-mounted hump case in Figure 3.3 was retrieved. The implemented WA model pressure and skin friction coefficient results and SA results taken from $flowPsi$ are presented with the reference data in Figure 3.4. One can observe that the $flowPsi$ slightly predicts more suction and underpredicts the skin friction on the hump surface for all three turbulence models compared to the reference, which is done using Ansys Fluent by Han et al. [7]. There are also small deviations in the separation zone for the SA model results. All of these differences are quite negligible for verification purposes since the trends are consistent with each other. The grid features and solver settings employed in these analyses may have contributed to the minor variances seen in Figure 3.4.

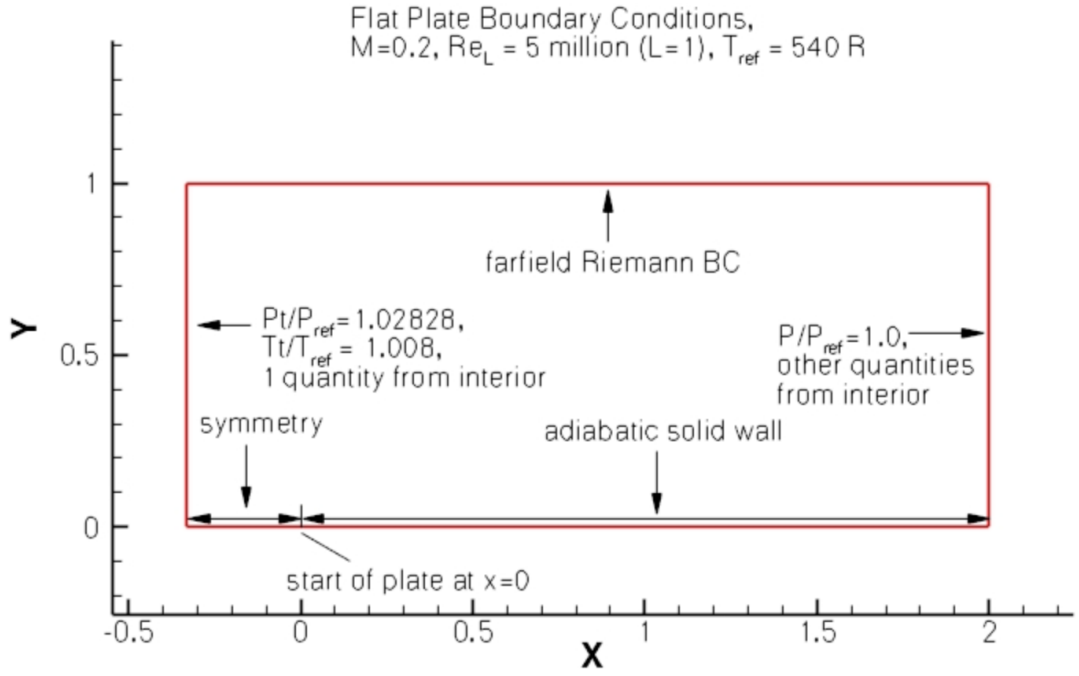

Figure 3.1: 2D Zero pressure gradient flat plate case. Retreived from [24]

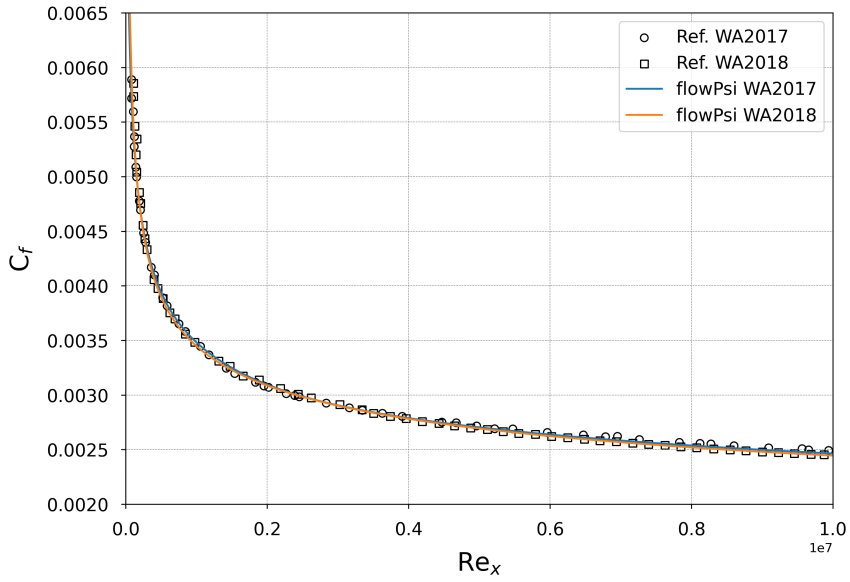

Figure 3.2: 2D Zero pressure gradient flat plate case results

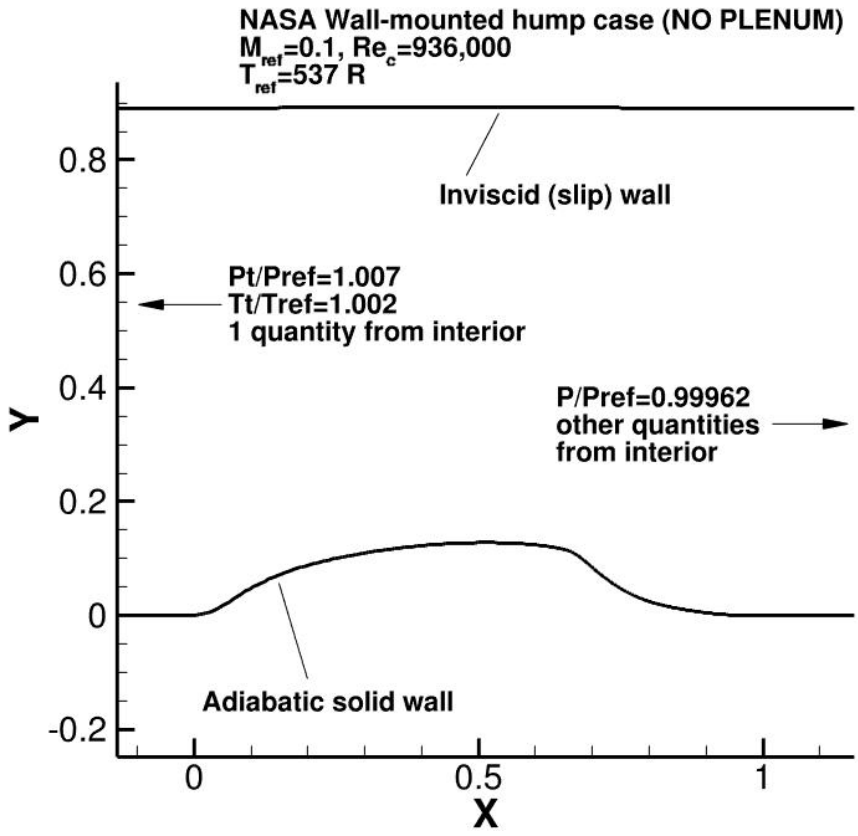

Figure 3.3: 2D Wall-mounted hump separated flow case. Retreived from [24]

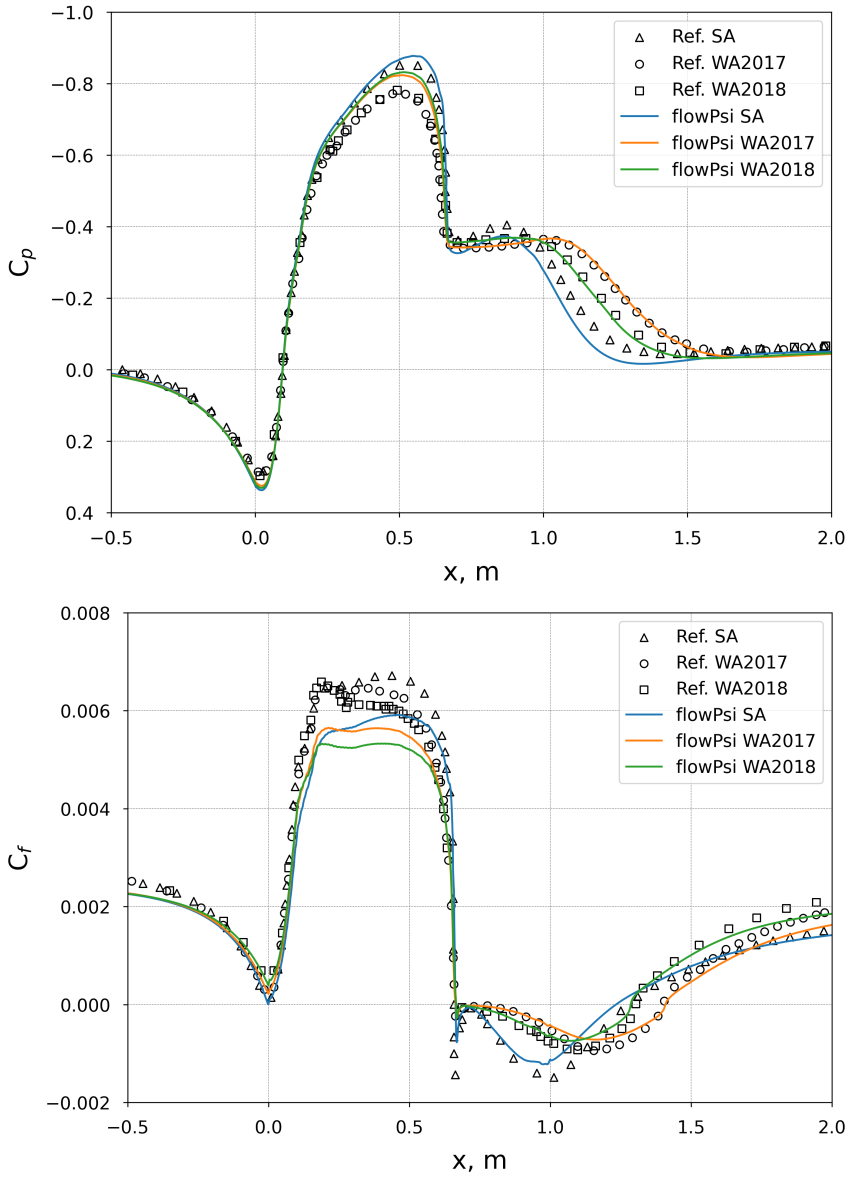

Figure 3.4: 2D Wall-mounted hump separated flow case result

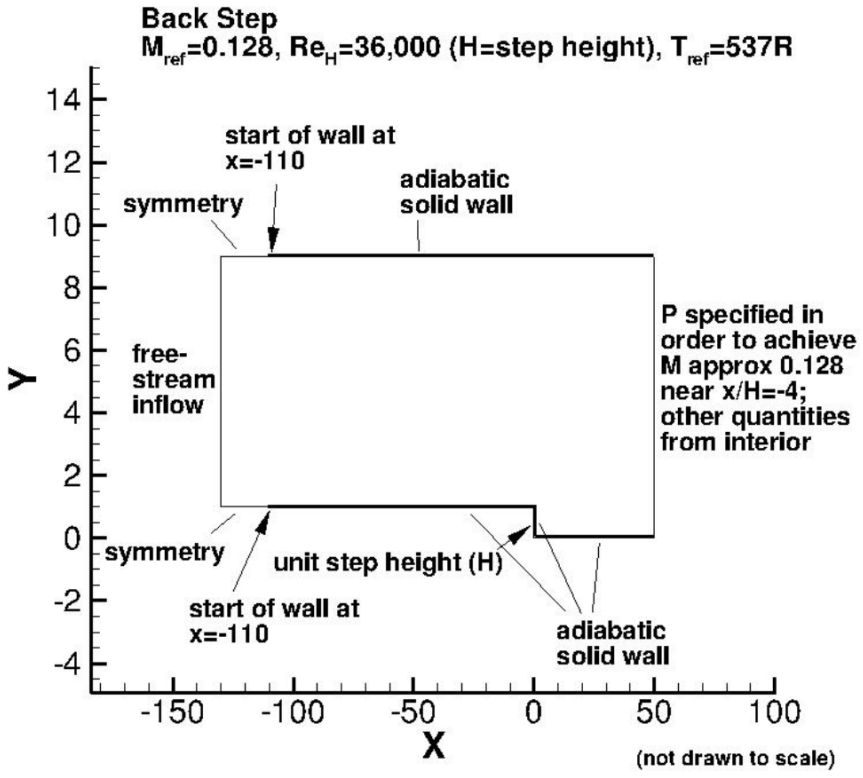

Figure 3.5: 2D Backward-facing step case. Retreived from [24]

3.1.3 Backward-Facing Step

The 2D backward-facing step case description in Figure 3.5 is obtained from the NASA Turbulence Modeling Resource webpage [24]. In this verification test case, both pressure and skin friction coefficients taken from the implemented WA models are compared to reference data in Figure 3.6. However, the WA2017 implementation in the $flowPsi$ code did not lead to a converged solution and kept oscillating. Therefore, only the comparison of WA2018 and SA models is provided in this section. Figure 3.6 shows excellent coherence for the implemented WA2018 model, which verifies our model implementation one more time.

3.2 Validation and Assessment of the Wray-Agarwal Model for SWBLI Flows

After the completion of the verification studies, compression ramp and impinging shock test cases with high deflection angles and various flow regimes are selected for

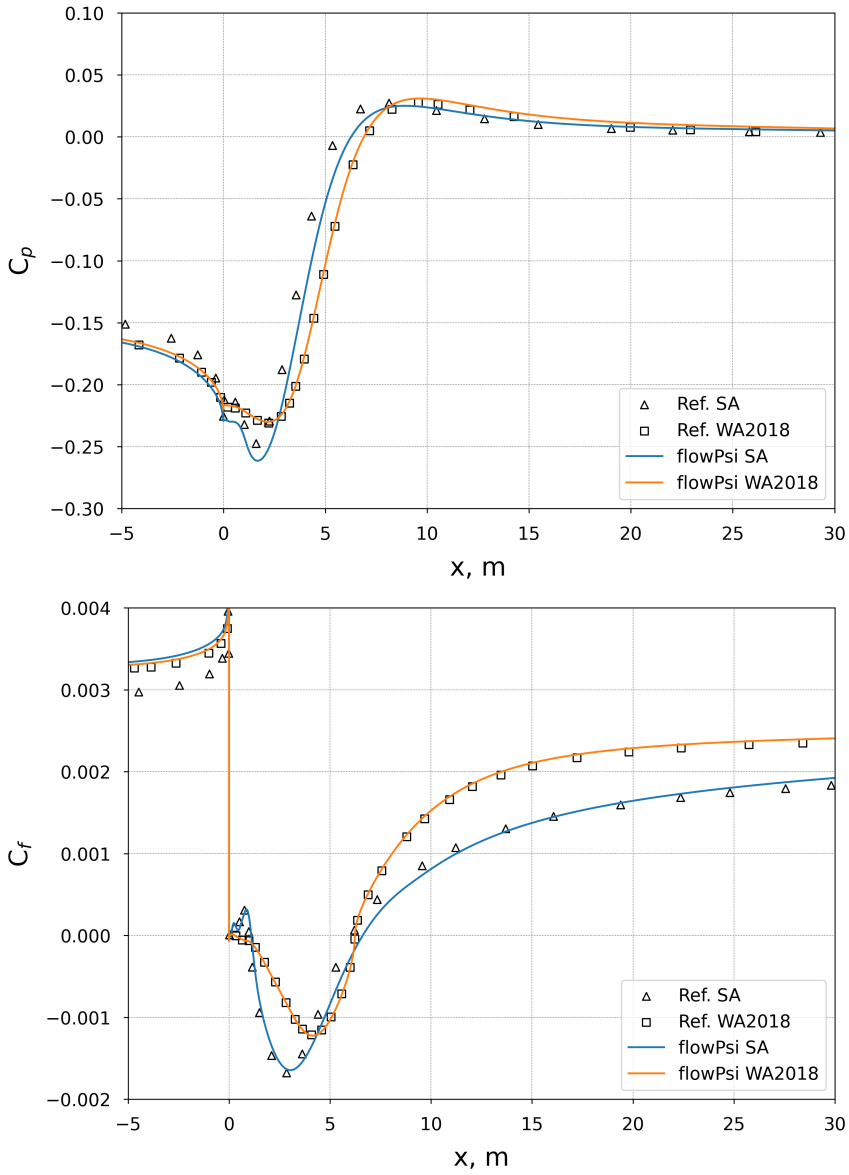

Figure 3.6: 2D Backward-facing step case results (Pressure coefficient on the left and skin friction coefficient on the right)

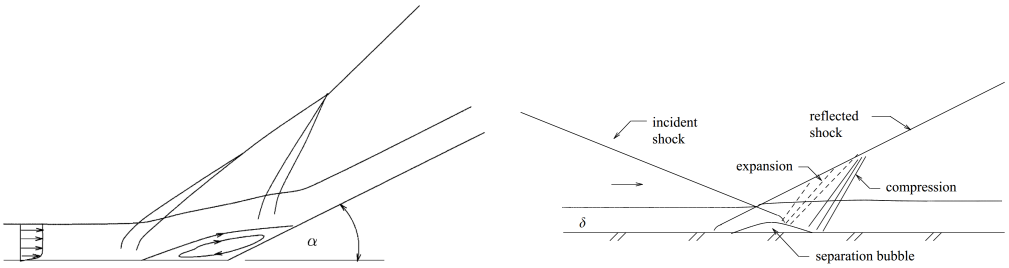

Figure 3.7: Flow structures of compression ramps on the left and impinging shocks on the right. Retreived from [36]

validation purposes. Standard turbulence models fail to predict the locations of separation and reattachment in these problem types. Thus, the aim is to clearly observe the modifications in the extended model. Therefore, standard validation test cases in SWBLI literature with high-deflection angles, as shown in Table 3.1, are chosen to assess the performance of the turbulence models.

In the Settles and Holden test cases, shock-separated turbulent boundary layers over compression ramps are investigated. The size of the separation is driven by the ramp angle in these compression ramp-type problems. The flow conditions were taken from the publications by Settles et al. [34] and Holden et al. [35].

The Schulein and Kussoy test cases investigate impinging shocks on turbulent boundary layers and their interactions. The interactions get stronger as the shock generator angle increases in these impinging shock cases. Figure 3.7 provides flow structures for both compression ramp- and impinging shock-type problems. The flow conditions for impinging shock test cases are taken from the publications by Schulein et al. [37] and Kussoy et al. [38]. Also, the experimental database prepared by NASA [39] is utilized to acquire SWBLI test conditions. Illustrations for both compression ramp and impinging shock problem types are shown in Figure 3.8.

Since the validation cases include hypersonic flows, the assumptions should be carefully made. We selected a solution strategy similar to those in the literature. We assumed that the ideal gas and Sutherland's viscosity law are valid for the selected validation cases.

A mesh independence study was carried out before the main investigations of this

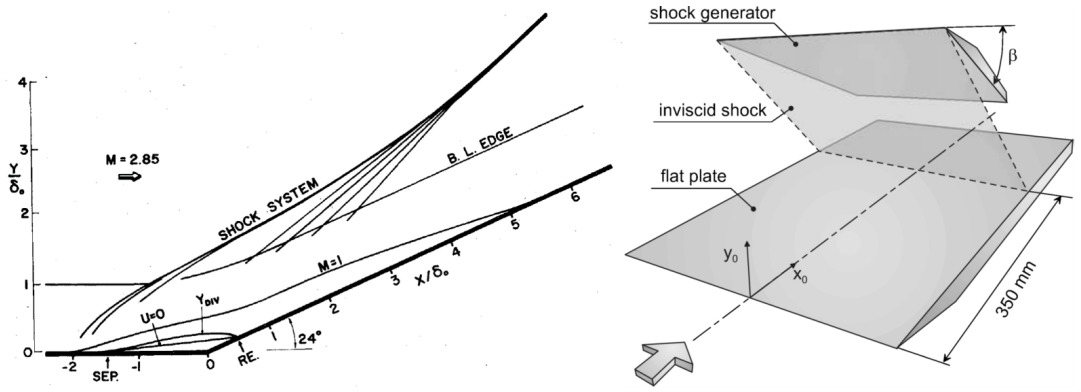

Figure 3.8: Settles compression ramp test case on the left and Schulein impinging shock test case on the right. Retreived from [34][37]

Table 3.1: Test cases

	$Angle\ [^o]$	M_∞	$P_0\,[kPa]$	$T_0\,[K]$	$T_w\,[K]$	Reference
Settles	24	2.84	690	262	$Adiabatic$	[34]
Schulein	6 10 14	5	2120	410	300	[37]
Holden	27 36	8.2	$1.2E5$ $1.15E5$	1027 1011	296 298	[35]
Kussoy	10	8.2	6080	1166	300	[38]

Table 3.2: Mesh independence details

		Coarse	Medium	Fine
Settles	Number of Grid Elem.	92732	165242	258552
	X-force $[N]$	48.37	48.12	48.03
Schulein	Number of Grid Elem.	49670	213065	307954
	X-force $[N]$	12.12	12.15	12.16
Holden	Number of Grid Elem.	62690	118420	237899
	X-force $[N]$	731	715	717
Kussoy	Number of Grid Elem.	27671	39498	78421
	X-force $[N]$	3.26	3.25	3.25

thesis. In the mesh independence study, three different cell sizes were generated. The mesh independence details are given in Table 3.2 where X-forces are calculated for viscous walls. The number of grid elements in coarse meshes is the lowest, whereas fine meshes have the greatest amount. Figure 3.9 shows the effect of different grid sizes on the results. It can be observed from Figure 3.9 that medium- and fine-resolution grids provide very similar wall pressure distributions in the domain. Also, Table 3.2 shows that medium- and fine-resolution grids result in very close X-forces. Therefore, we selected medium-resolution grids since they have comparable accuracy to fine-resolution grids with a smaller number of grid elements, which results in efficiency in computational effort. Also, average wall y^+ values for each mesh are less than 1 for all cases.

Section 3.2.1 provides the mesh figures corresponding to the mesh independence study for each test case. Settles' test case is used for the preliminary works of this thesis, and we generated structured-type meshes for this test case. After different validation cases were added to the study, we switched to unstructured-type meshes since it is easier to generate unstructured meshes than structured ones.

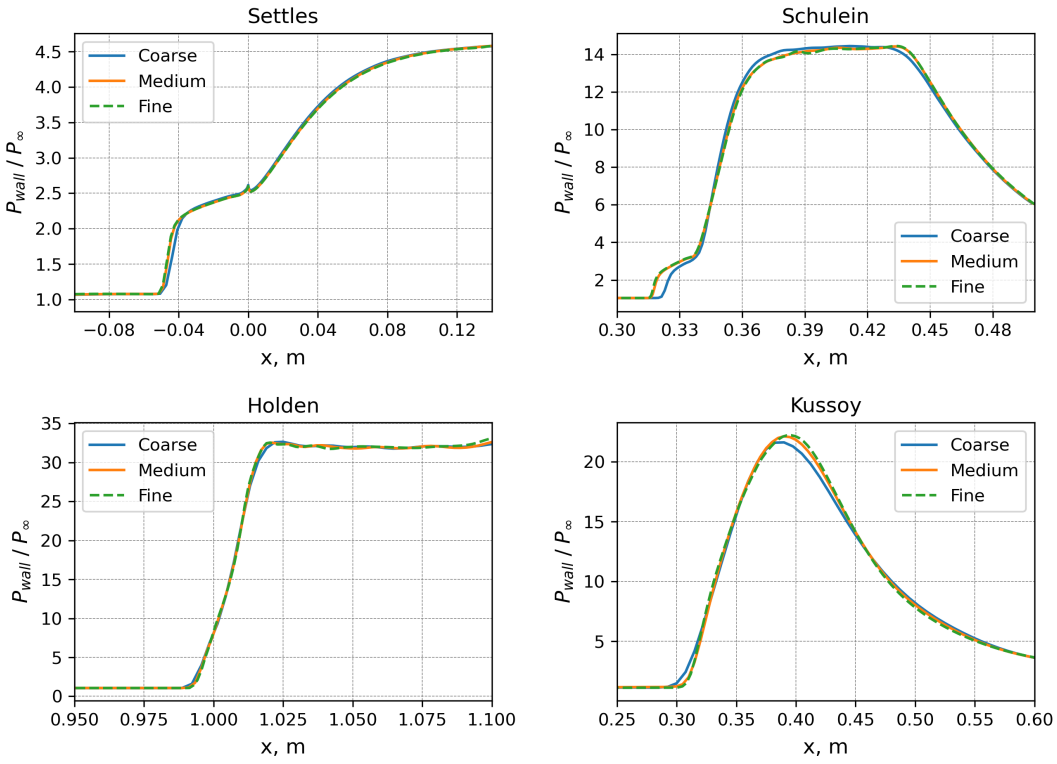

Figure 3.9: Mesh independence results on validation cases

3.2.1 Assessment of Wray-Agarwal Model

In this section, the standard formulations of the Wray-Agarwal turbulence models are evaluated alongside the Spalart-Allmaras model.

3.2.1.1 Settles' Test Case

This thesis compares turbulence models by examining pressure distributions on several test cases. Since separations induced by shock wave-boundary layer interactions are the primary focus of the study, the locations of separation and reattachment alongside the recirculation zone, which is illustrated in Figure 3.10, are investigated. When the shear stress or skin friction coefficient undergoes a sign change from positive to negative, the flow becomes separated. Conversely, the reattachment point is indicated by a sign shift from negative to positive. Between separation and reattachment points, the skin friction coefficient is negative, which shows the recirculation zone.

Starting with the Settles' test case, the problem description is given in Figure 3.11. In Settles' experimental research paper [34], it is stated that the walls are adiabatic. Therefore, we assumed the walls to be adiabatic as well. For inflow boundary condition (BC), supersonic inflow BC was used with pressure, temperature, and Mach number values. The supersonic outflow BC was used for the outlet, and no information is needed for this type of BCs.

The mesh details are presented in Figure 3.12 for Settles' test case. To make solutions independent from the grid, a mesh independence study was performed with three different meshes. For each step, the grid sizes were reduced, and finer meshes were generated, as seen in Figure 3.12. The medium-resolution grid was used for the remaining CFD analyses, as mentioned in Section 3.2.

The normalized wall pressure and skin friction coefficient distributions of the 2.84 Mach 24^o ramp angle Settles' compression ramp test case are given in Figure 3.13. It can be observed from the figure that the WA2018 model performs better than the WA2017 model, whereas the SA model is superior to both WA models in terms of separation location and recirculation zone size estimations in this case. The Wray-

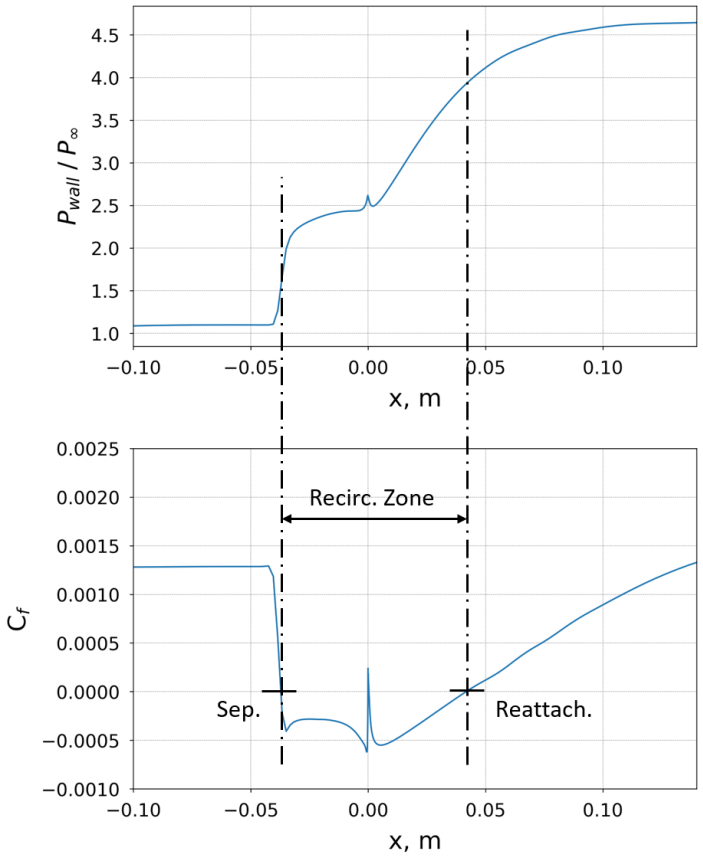

Figure 3.10: Separation, reattachment, and recirculation zone illustration on Settles' test case

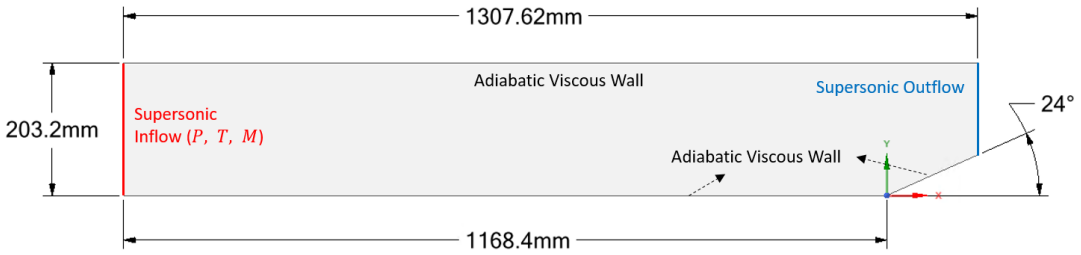

Figure 3.11: Problem description of Settles' test case

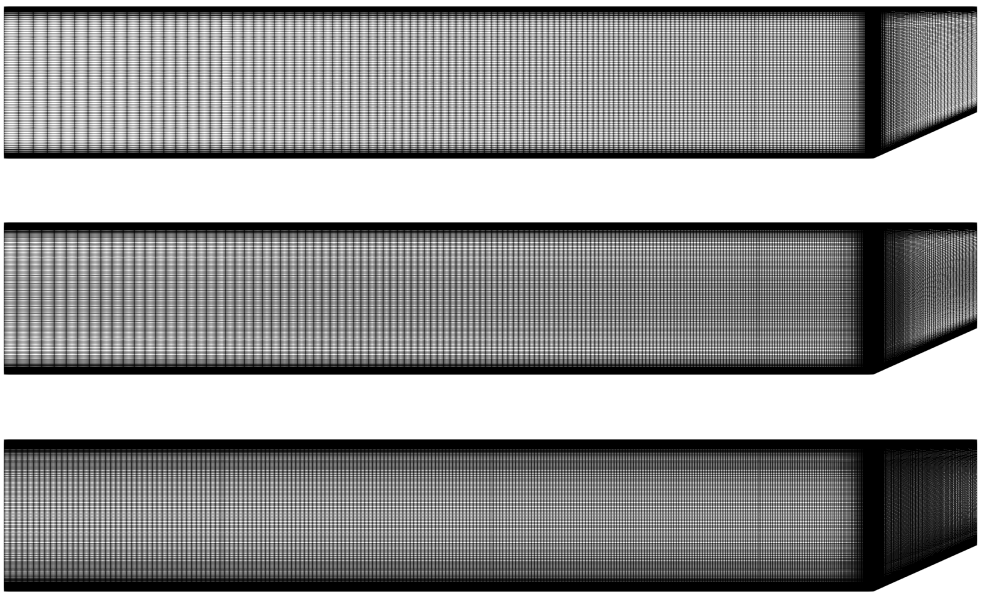

Figure 3.12: Mesh independence study on Settles' test case

Agarwal models predict earlier separation with a larger recirculation zone compared to experimental data.

3.2.1.2 Schulein's Test Case

Figure 3.14 presents the problem description of Schulein's test cases. The θ shows the shock generator angle. Also, the shock generator was located in a way that inviscid shock impinges to $x = 350\ mm$ for each shock generator angle, which is illustrated in Figure 3.8. Therefore, the distance of the shock generator angle, L, has three different lengths for three different shock generator angles. The outlet size was also driven by the shock generator angle, as can be seen in Figure 3.14. Similar to previous validation case, supersonic inflow and outflow BCs were used. The walls were set to viscous walls with a constant temperature of $300\ K$.

The grids used in the mesh independence study of Schulein's test case are given in Figure 3.15. The grid element sizes are reduced after the shock generator wall since the first part of the domain is mostly uniform before the shock. Therefore, mesh is refined in the region of interest, which results in a smaller mesh size increase.

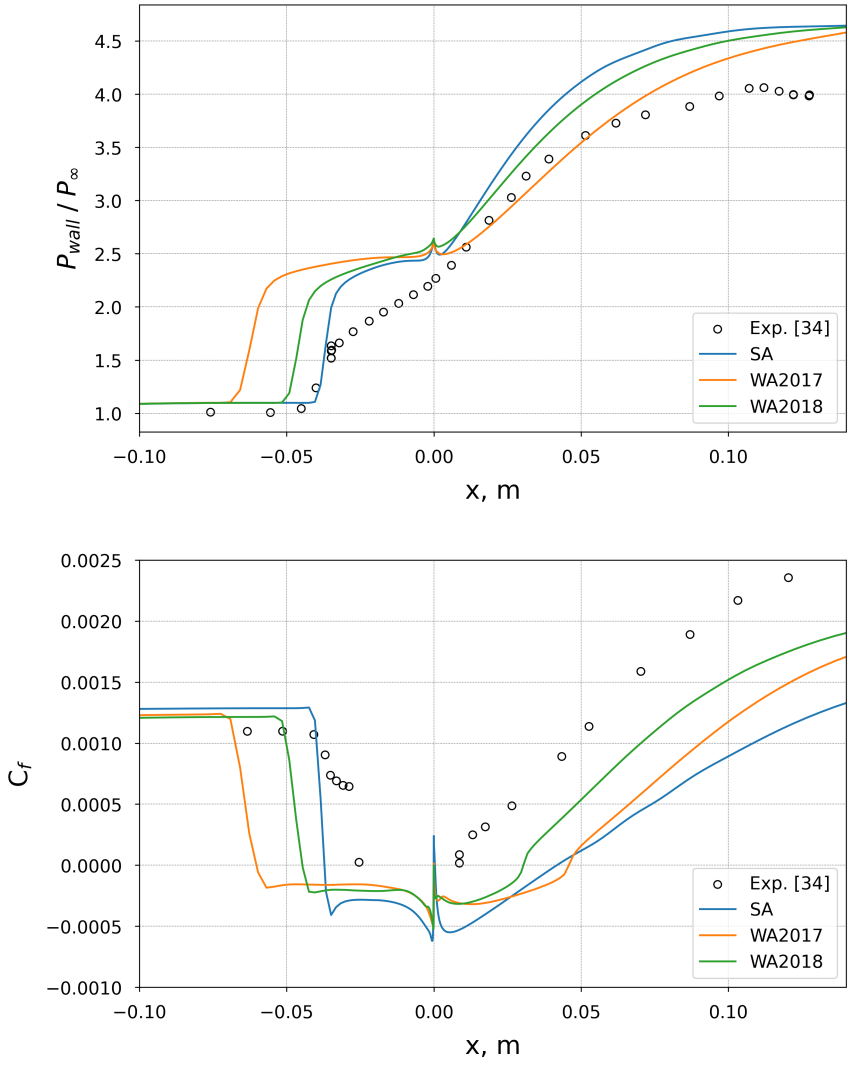

Figure 3.13: Settles 24^o compression ramp test case results

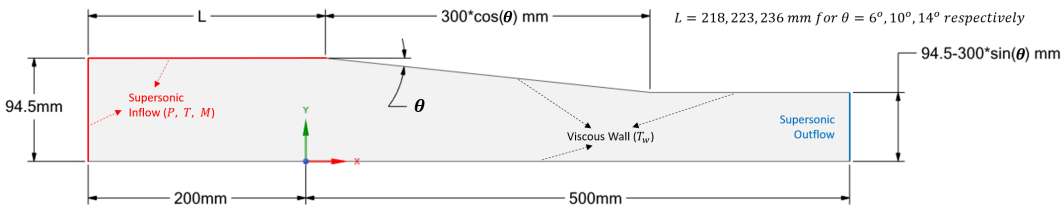

Figure 3.14: Problem description of Schulein's test cases

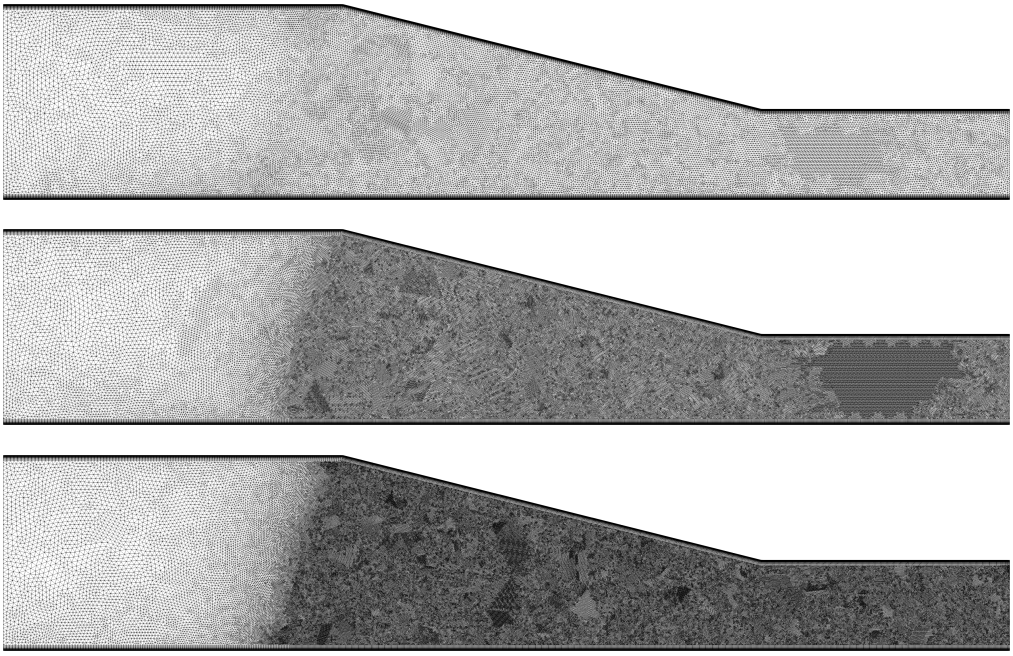

Figure 3.15: Mesh independence study on Schulein's test case

The computation results and experimental data of 5 Mach, Schulein's impinging shock test case with three different shock generator angles ($\beta = 6^o$, 10^o, and 14^o) are shown in Figure 3.16 and 3.17. The experimental shear stress data were not available for 6^o shock generator angle case. The reference SA and $k - \omega$ SST results, which were obtained from the literature, are also added for this test case. We confirm once more that our solutions are independent of mesh and consistent with the other CFD results from the literature by comparing the reference and $flowPsi$ SA results.

In Schulein's test case, the recirculation region enlarges with increasing shock generator angles since the interaction between the shock wave and boundary layer gets stronger, and turbulence models begin to fail to predict the separation locations. In the 6^o shock generator angle case, all turbulence models give excellent surface pressure distribution predictions compared to experimental data. In the 10^o shock generator angle case, a small recirculation zone starts forming, which can be observed from experimental data. The WA models have a great agreement with the experimental data, while the SA model fails to catch the separation for 10^o shock generator angle. In the 14^o shock generator angle case, however, each model behaves differently in the recir-

culation region. It is observed that the WA2017 model provides the best consistency with the experimental data. The WA2018 model predicts slightly delayed separation, but it still outperforms the SA model, which predicts separation location more downstream and a small recirculation zone compared to experimental data. To sum up, the WA models are superior to the SA model in terms of predicting SWBLIs for 5 Mach impinging shock cases.

3.2.1.3 Holden's Test Case

The problem description of Holden's test case is presented in Figure 3.18. In this compression ramp problem, the walls were configured to be viscous with a constant temperature of $296K$ and $298K$ for 27^o and 36^o ramp angles, respectively. Supersonic inflow and outflow boundary conditions were selected for this problem as well.

The illustrations of the grid refinement study of Holden's test case are given in Figure 3.19. In this case, the surroundings of the ramp were refined since the high gradients due to shock are generated in this region.

In Holden's 8.2 Mach compression ramp test, different ramp angles were examined, starting from no-separation/attached flow to fully separated flow using the medium-resolution grid. In this study, 27^o and 36^oramp angles were selected for assessment of the turbulence models. In this regard, the normalized pressure and shear stress distributions of 27^o and 36^o compression ramps are given in Figures 3.20 and 3.21, respectively.

Firstly, each model predicts similar wall pressure distributions for the 27^o ramp angle case, where no separation is observed. In the 36^o ramp angle case, the WA2017 model gives an unrealistically early separation estimation. On the other hand, the WA2018 and SA models predict close pressure distributions compared to the experimental data where the WA2018 overpredicts and the SA underpredicts the recirculation zone size. Thus, the WA2018 and SA models are superior to the WA2017 model in Holden's hypersonic compression ramp.

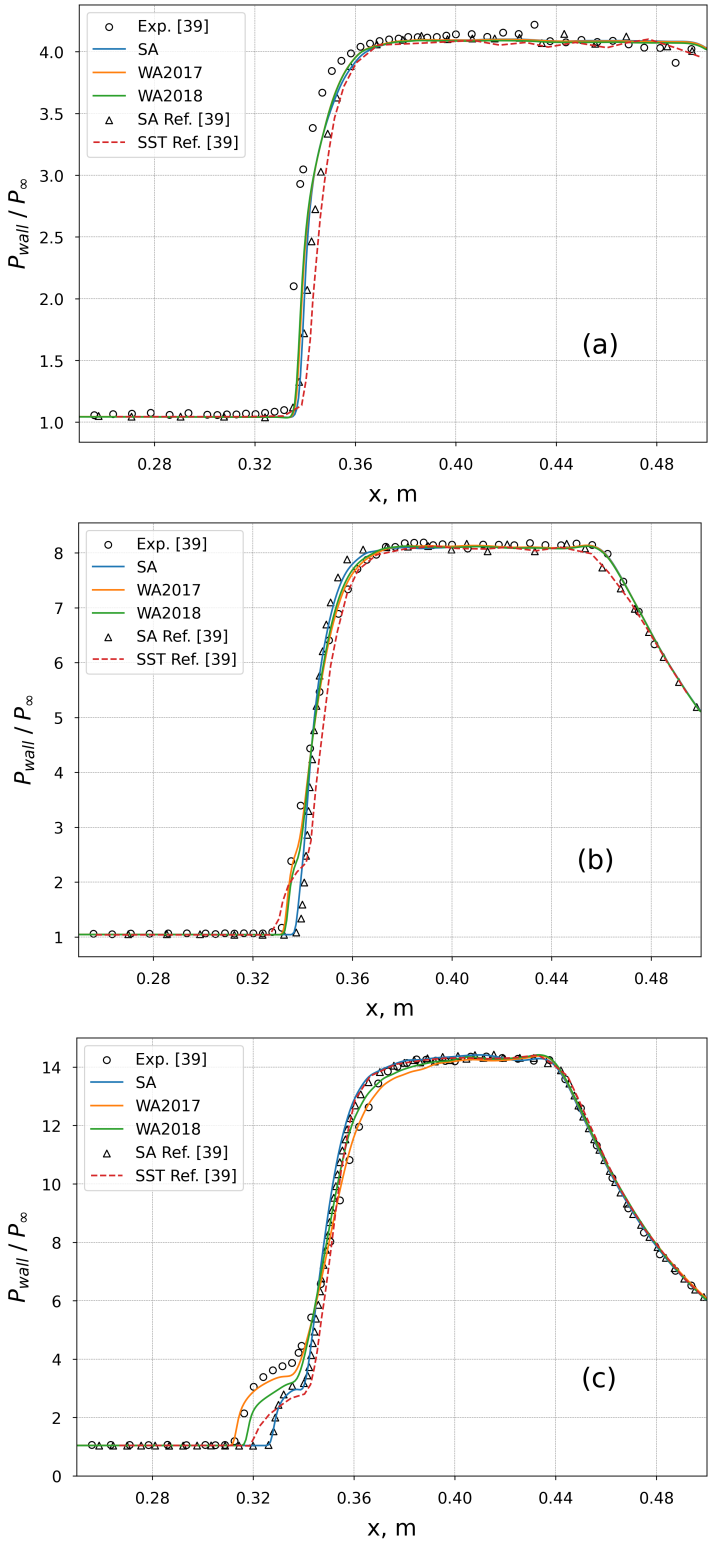

Figure 3.16: Schulein impinging shock test case wall pressure results for (a) $\beta = 6^o$, (b) $\beta = 10^o$, and (c) $\beta = 14^o$

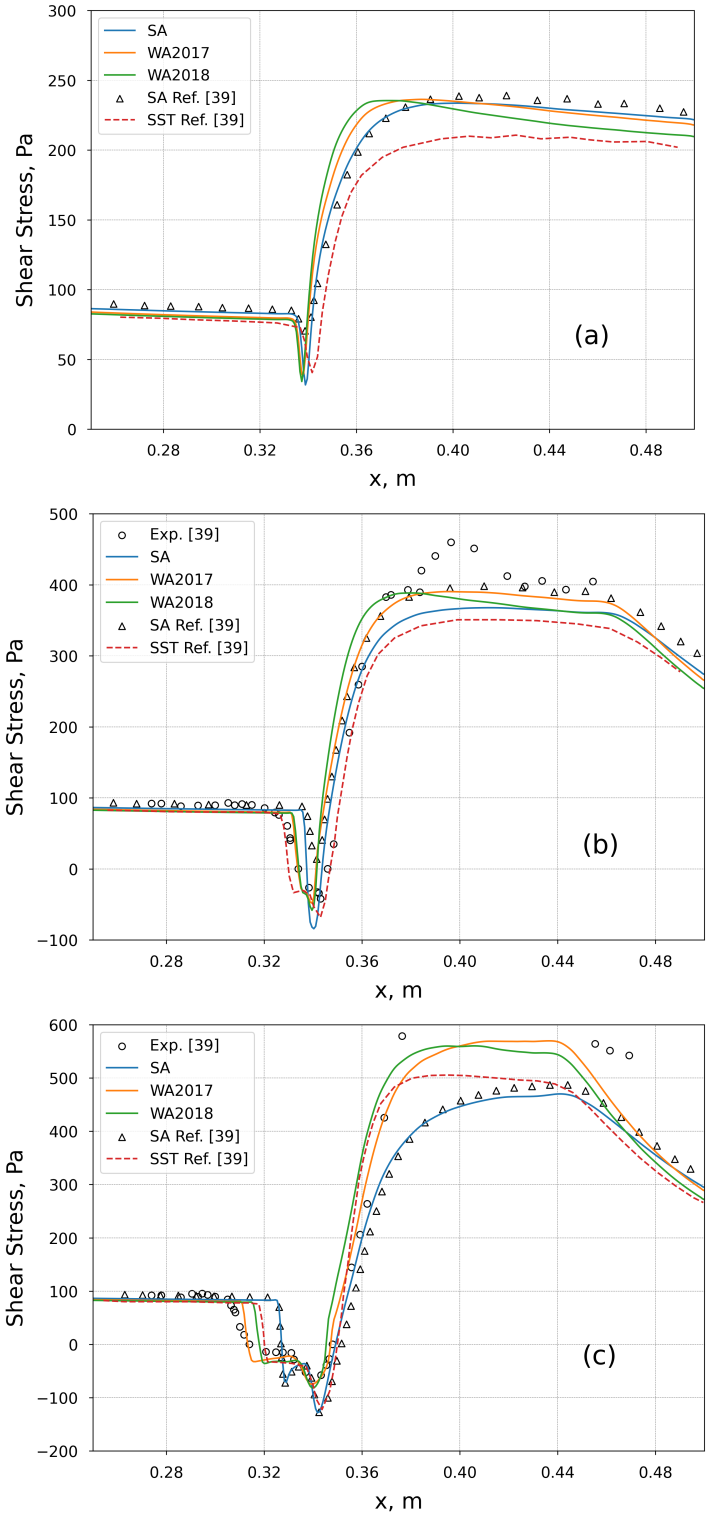

Figure 3.17: Schulein impinging shock test case shear stress results for (a) $\beta = 6^o$, (b) $\beta = 10^o$, and (c) $\beta = 14^o$

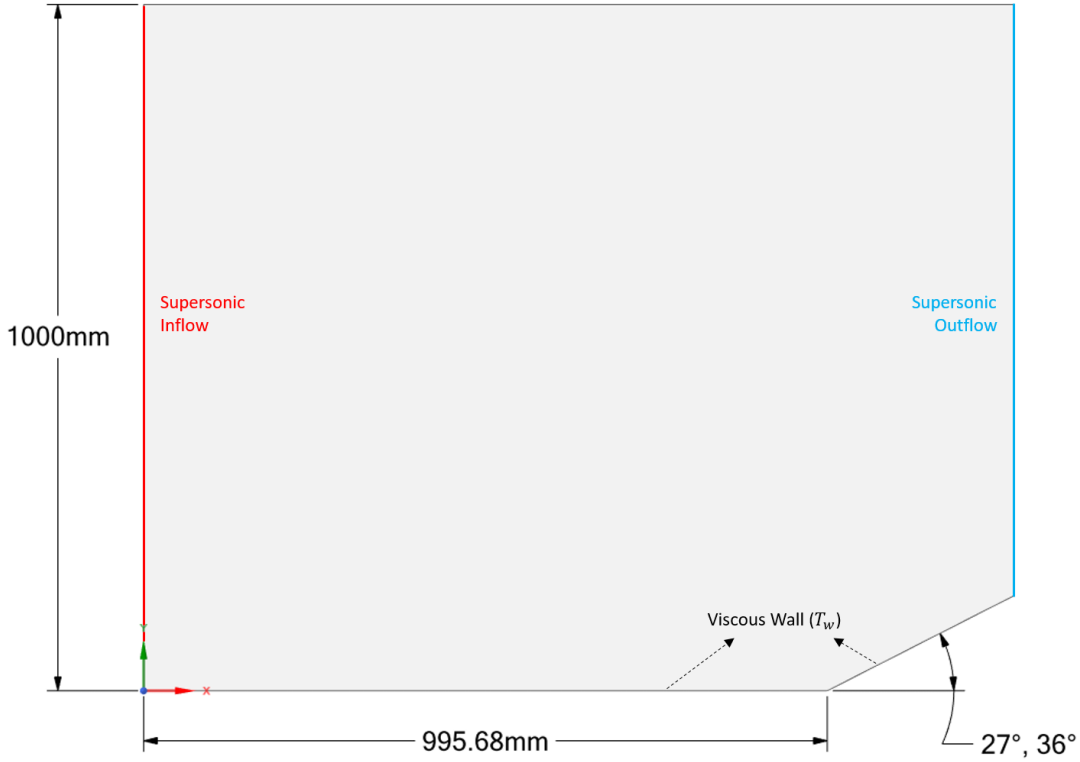

Figure 3.18: Problem description of Holden's test cases

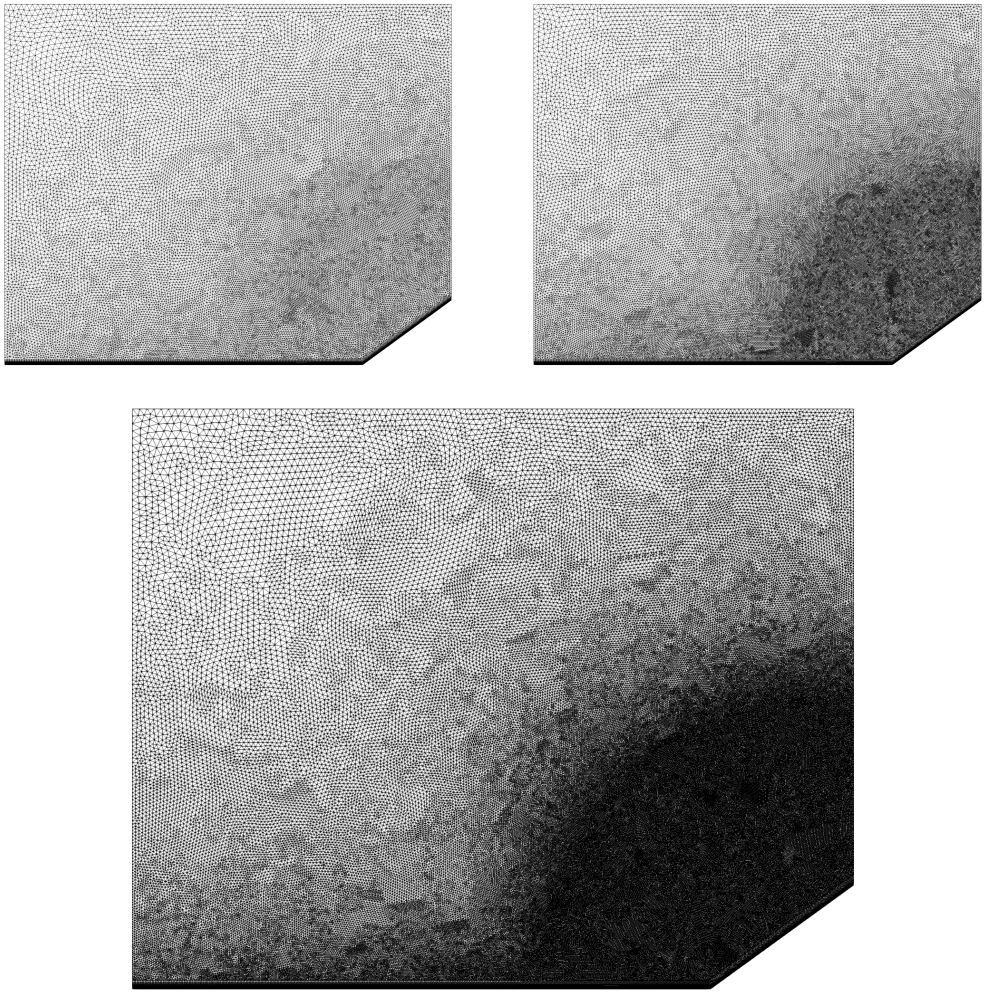

Figure 3.19: Mesh independence study on Holden's test case

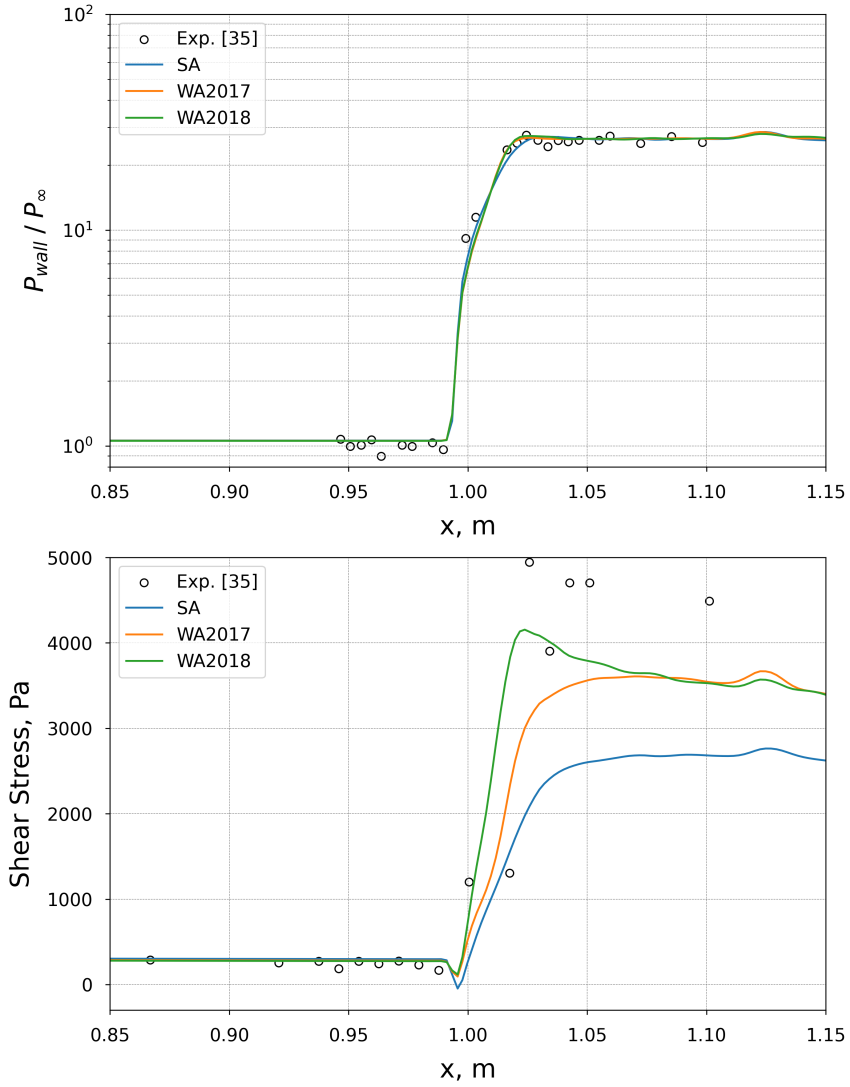

Figure 3.20: Holden compression ramp test case results for 27^o ramp angle

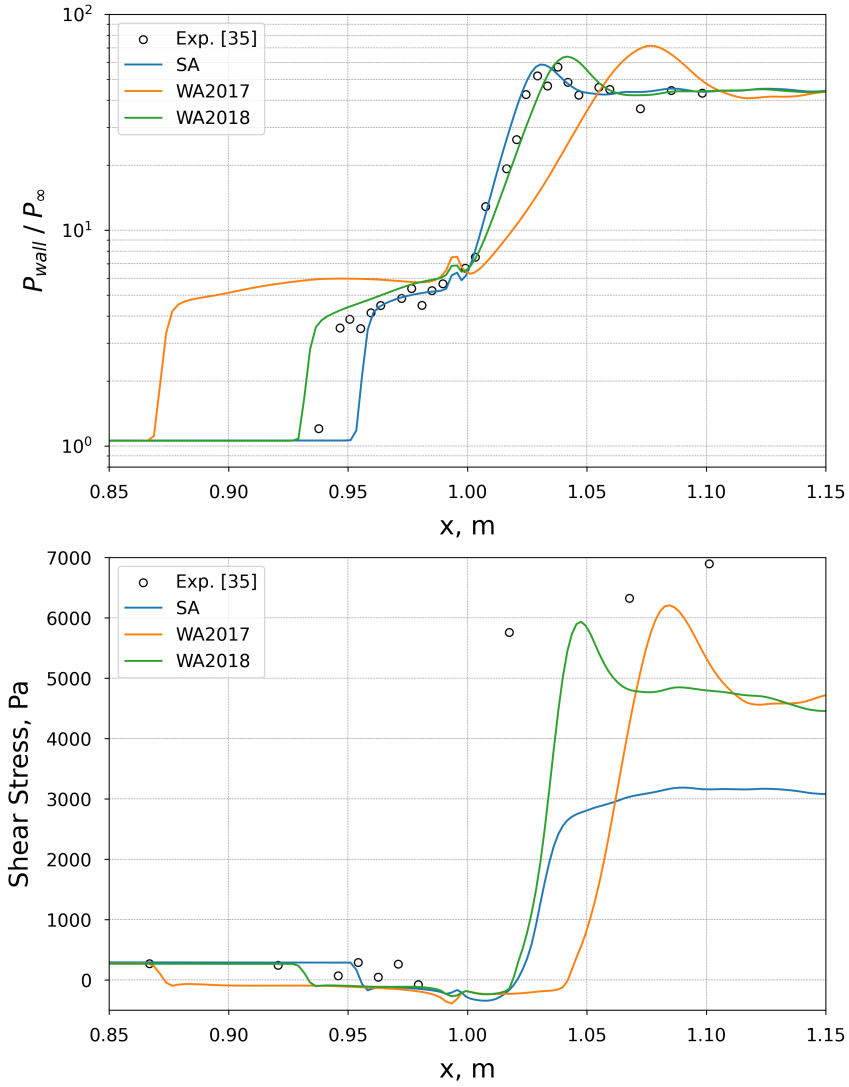

Figure 3.21: Holden compression ramp test case results for 36^o ramp angle

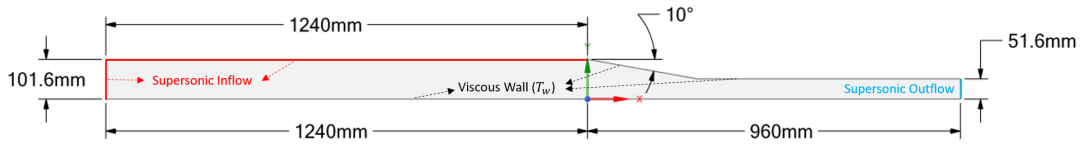

Figure 3.22: Problem description of Kussoy's test case

3.2.1.4 Kussoy's Test Case

The illustration of the problem setup is given in Figure 3.22. The shock generator angle is 10^o for this impinging shock test case. The constant temperature of $300\ K$ was set to viscous walls. Supersonic inflow and outflow boundary conditions were applied for this test case.

The meshes used in the mesh independence study of Kussoy's test case are given in Figure 3.23. The meshes were gradually refined for each step. Since the medium- and fine-resolution grids provided similar results, which can be seen in Figure 3.9, the medium-resolution grid has been selected for further analysis.

The CFD results of Kussoy's 8.2 Mach impinging shock test case with a 10^o shock generator angle are given in Figure 3.24. In this hypersonic impinging shock test case, all one-equation turbulence models predict similar distributions. Even though these predictions are close to the experimental results overall, all of the one-equation turbulence models fail to estimate the separation. In contrast, the $k-\omega$ SST model captures the separation and outperforms the one-equation models overall, agreeing more with the experimental data. Similar behavior would have been expected from the WA model since it is a $k-\omega$ based one-equation model; however, the WA model also fails to find the separation in this test case.

3.2.2 Performance of the Standard Wray-Agarwal Model for Heat Flux Predictions

In this study, it is observed in all test cases that the WA model performs poorly on heat flux predictions compared to both the SA model and experimental data. Other turbulence models and experimental data do not agree with the WA model's unphysical

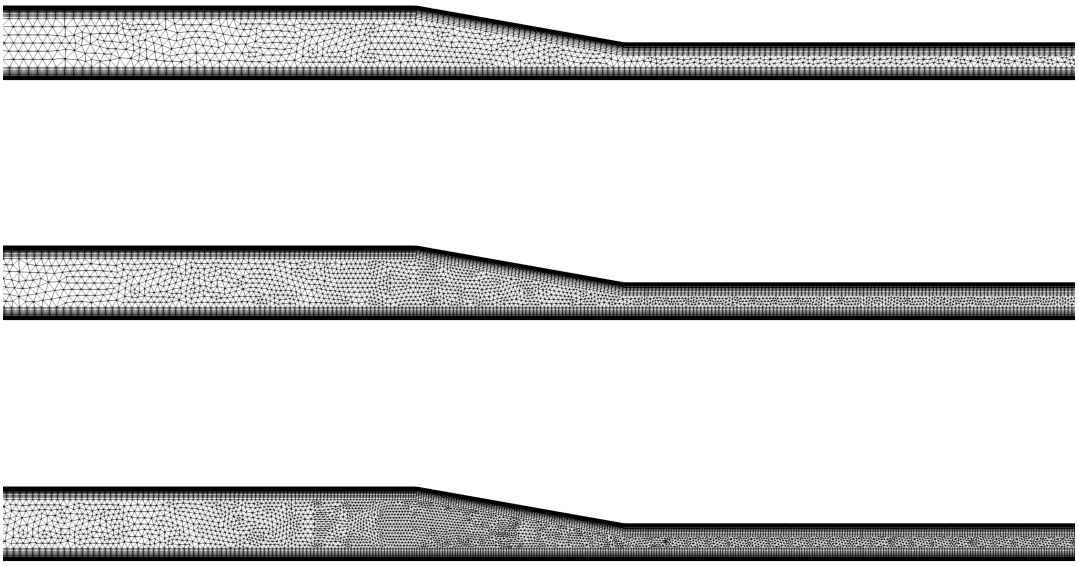

Figure 3.23: Mesh independence study on Kussoy's test case

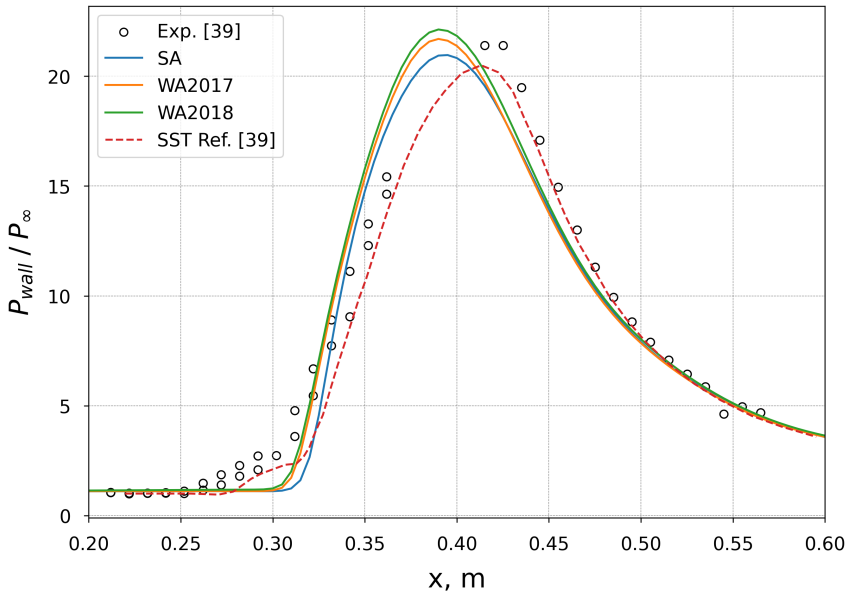

Figure 3.24: Kussoy 10^o shock generator angle impinging shock test case results

prediction of an abrupt spike followed by a sharp reduction in the heat flux distribution. Also, the WA model generally overestimates the values of heat fluxes. This can be seen from Figures 3.25, 3.26, and 3.27. Additional research is necessary to determine the cause of this behavior. The effect of first layer thickness on the results would be a logical investigation for heat flux predictions as future work.

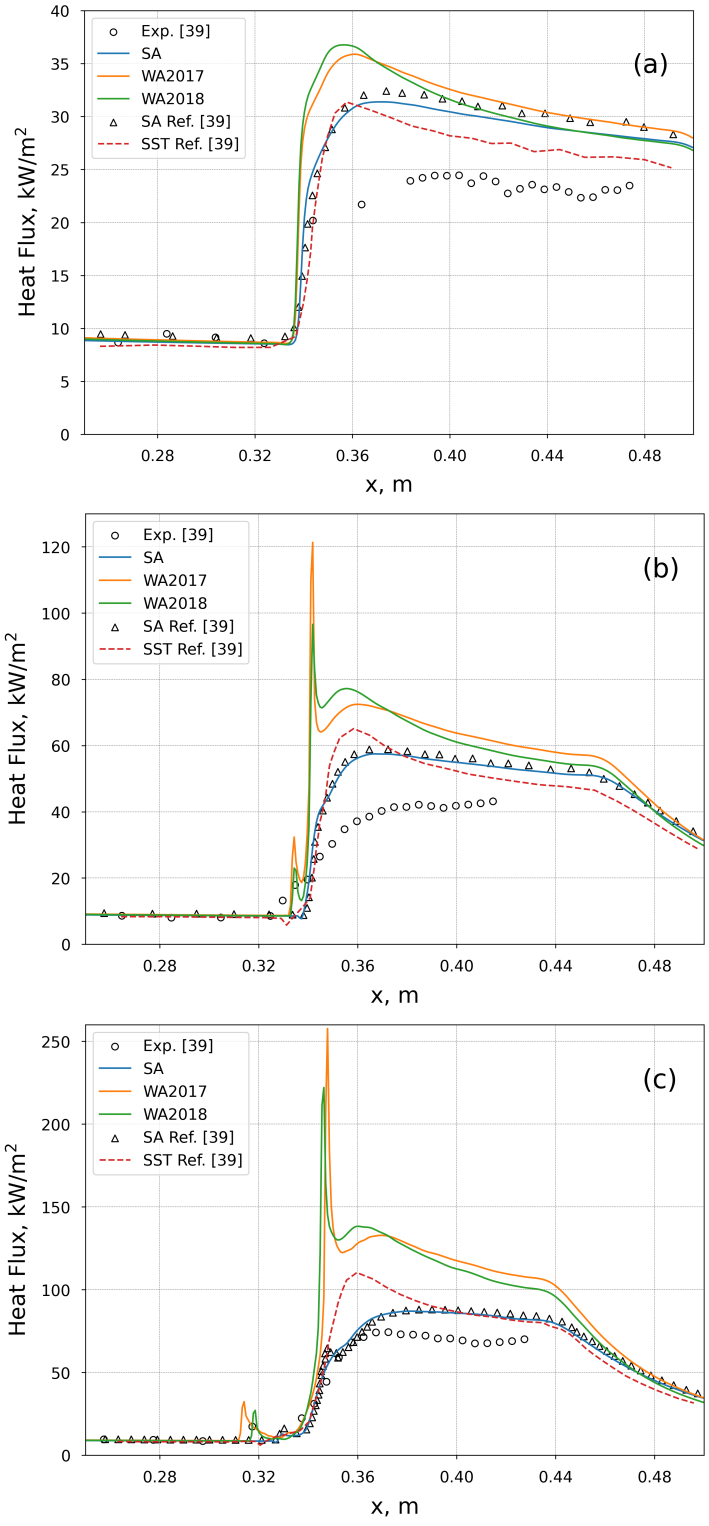

Figure 3.25: Schulein impinging shock test case heat flux results for (a) $\beta = 6^o$, (b) $\beta = 10^o$, and (c) $\beta = 14^o$

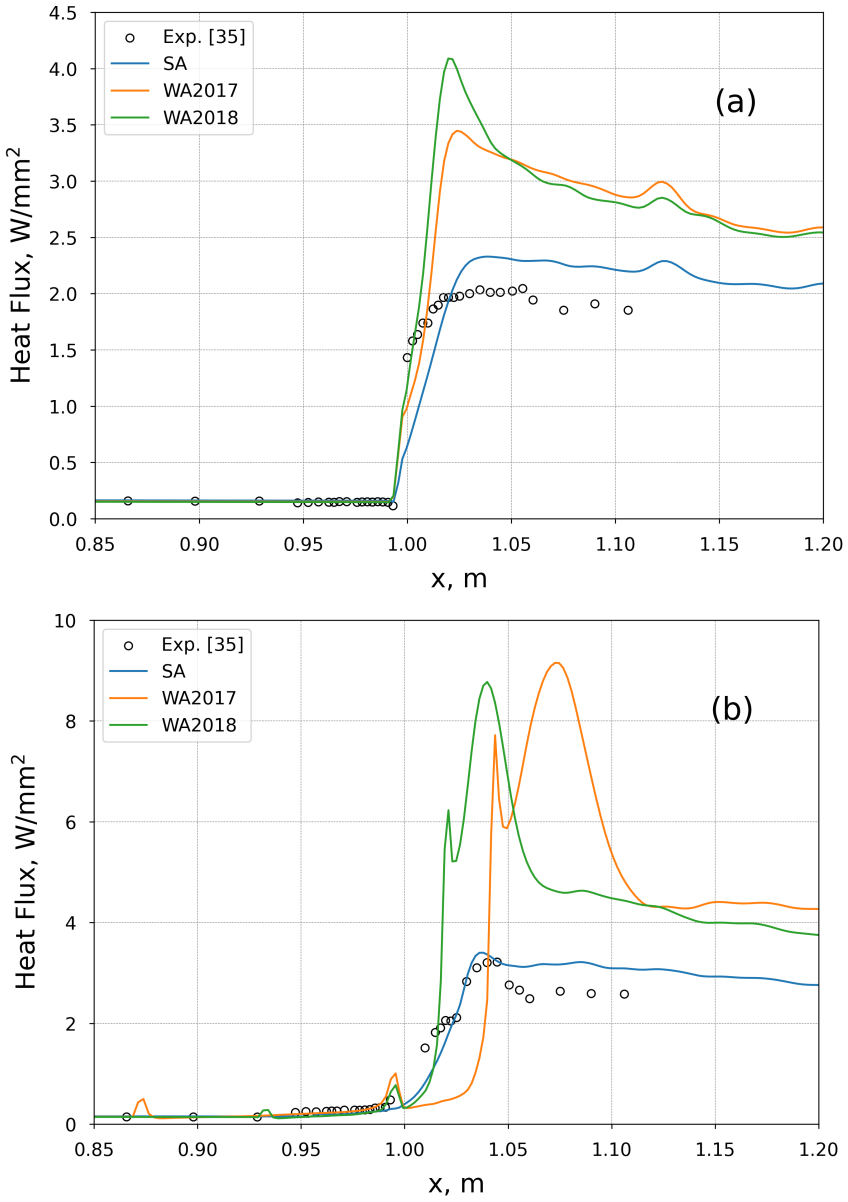

Figure 3.26: Holden compression ramp test case heat flux results for (a) 27^o and (b) 36^o ramp angles

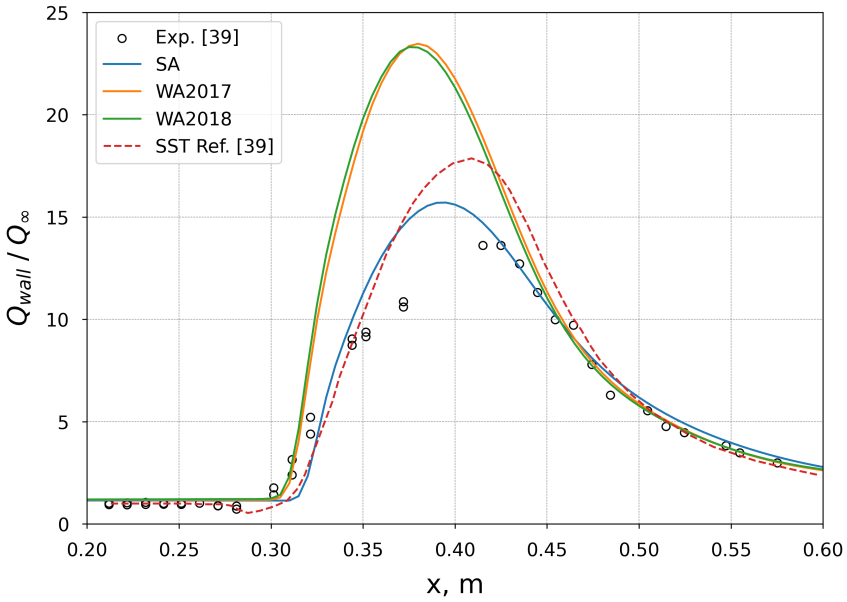

Figure 3.27: Kussoy 10^o shock generator angle impinging shock test case heat flux results

CHAPTER 4

EXTENSION OF THE WRAY-AGARWAL 2018 TURBULENCE MODEL FOR SWBLI FLOWS

4.1 Theory of Current Modifications on the WA2018 Model

In this section, the adaptation of the potential enhancements from the literature to the Wray-Agarwal model is explained. The WA2018 version was selected for modification attempts since it performs better than the WA2017 model, as shown in Section 3.2. Also, the ease of implementation and lower computational cost of the WA2018 model caused by the elimination of wall-distance calculations are other motivations for selecting the WA2018 model over the WA2017 model for this study.

4.1.1 Shock Unsteadiness Model

As a first attempt to improve the performance of the WA2018 model in SWBLIs, we adapted the improvements developed by Sinha [25], which are briefly explained in Section 2.2.1.

Similar to the study of Sinha [25], we modify the production term of the Wray-Agarwal 2018 turbulence model to suppress the amplification of turbulent kinetic energy k. Since the transport equation of R is defined as $R = k/\omega$ where ω can be written as $\omega = \varepsilon/k$, the R or ν_T is proportional to k^2/ε, same as the Spalart-Allmaras modification. Therefore, we replaced C_1 in the production term of Eq. (2.7) with $C_1^{'}$, which is defined in Eq. (4.1)

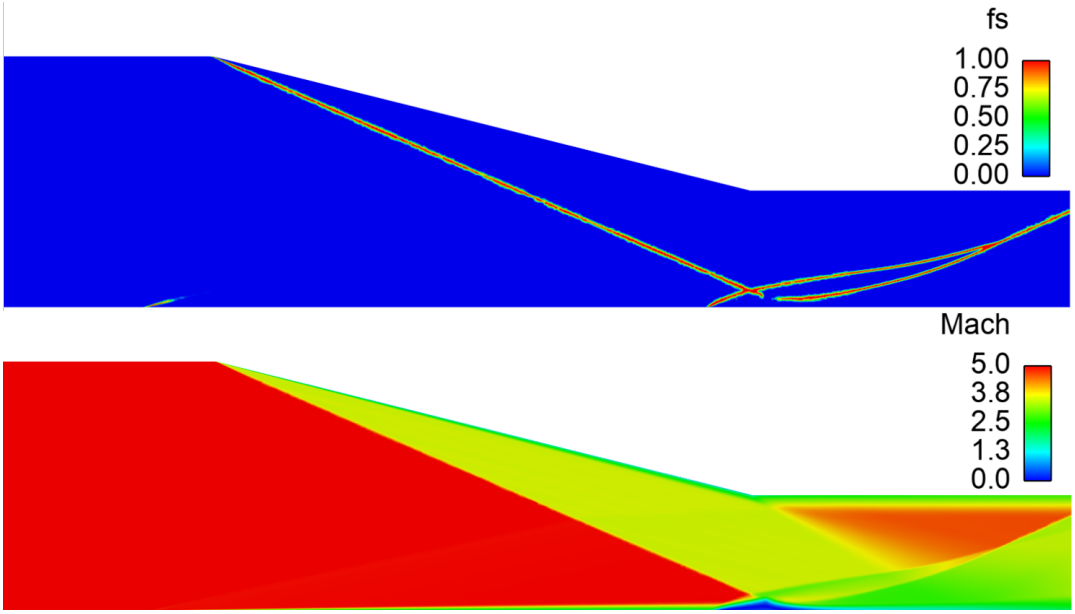

Figure 4.1: Switching function and Mach number contour of Schulein's 14^o test case

$$C_1^{'} = \frac{4}{3}\left(1 - b_1^{'}\right) - \frac{2}{3}c_{\varepsilon 1} \tag{4.1}$$

where $b_1^{'}$ and $c_{\varepsilon 1}$ are given in Eq. (2.18). As mentioned in Section 2.2.1, modifications should be used only in locations of strong dilation. The f_s in Eq. (2.31) is utilized to find the shock waves where the modification is only applied to the production term. Example contours related to f_s and Mach number can be observed from Figure 4.1.

The production term of the WA2018 transport equation, which is given in Eq. (2.7), is modified such that it switches to $C_1^{'}$ in strong dilation regions (Eq. (4.2)).

$$Production = (1 - f_s)\, C_1 RS - f_s C_1^{'} RS_{ii} \tag{4.2}$$

The relation given in Eq. (2.19) is implemented into the code since there is a need for the upstream Mach number normal to the shock wave, M_{1n}, inside the Eqs. (4.1) and (2.18). One can consider applying the inviscid shock relations for the estimation of the upstream Mach number normal to the shock wave, yet this approach would be inaccurate due to viscous flow occurring in, e.g., boundary layers. Therefore, we decided to implement the aforementioned equations to obtain the upstream Mach

number normal to the shock wave. The computed upstream Mach number normal to the shock wave is utilized to calculate the variables in Eq. (2.18).

The extended WA2018 model with shock unsteadiness modification is designated as WA2018SU in the following sections.

4.1.2 Reynolds Anisotropy Inclusion

In this part, we propose a potential improvement on the SWBLI simulation capabilities of the WA2018 model based on Raje and Sinha's model. For this purpose, the eddy viscosity definition of the original WA2018 model is scaled with C_μ^*/C_μ term. Raje and Sinha used $F_2^{'}$ in Eq. (2.30) to identify turbulent boundary layers and shock waves. Similarly, we utilized f_1 in Eq. (2.13) and $F_1^{'}$in Eq. (4.3) for blending between the anisotropy introduced and standard eddy viscosity definitions. To avoid changing the behavior of the WA2018 model in the viscous sublayer and buffer layer, we applied blending rather than directly multiplying the anisotropy parameter by the eddy viscosity. We illustrate the behavior of f_1 in Figure 4.2. As seen in this figure, f_1 equals unity within the viscous sublayer and buffer layer. Then, it drops to 0.06 in the log-law region.

It is anticipated that the factorization by the anisotropy parameter, C_μ^*, in Eqs. (2.28) and (2.29) will lead to improvements as both alternative denominators of Eq. (2.30) contain C_μ^* directly or implicitly via a_1^*.

We applied C_μ^*/C_μ scaling in two different methods in the WA2018 eddy viscosity definition to observe the effect of the anisotropy parameter in the vicinity of shock waves. In the first method, scaling is done only across the turbulent boundary layer using f_1, whereas it is applied across both the turbulent boundary layer and shock waves using $F_1^{'}$ in the second method. We designate these methods as WA2018S-1 and WA2018S-2, respectively. The eddy viscosity definition for each method is given in Eqs. (4.4) and (4.5).

$$F_1^{'} = min(f_1, 1 - f_s) \tag{4.3}$$

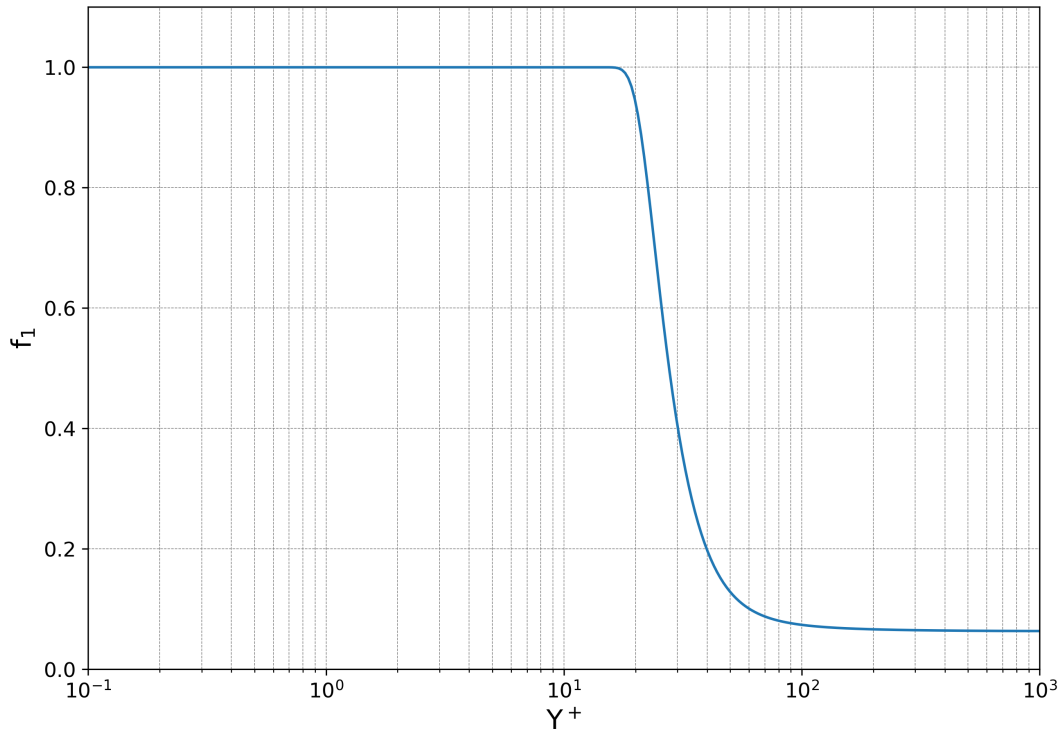

Figure 4.2: Variation of f_1 across the flat plate boundary layer

$$\nu_{T_{2018S-1}} = (1 - f_1)\, f_\mu R \frac{C_\mu^*}{C_\mu} + f_1 f_\mu R \tag{4.4}$$

$$\nu_{T_{2018S-2}} = \left(1 - F_1^{'}\right) f_\mu R \frac{C_\mu^*}{C_\mu} + F_1^{'} f_\mu R \tag{4.5}$$

One can see the qualitative difference between f_1 and $F_1^{'}$ in Figure 4.3. To make sure that the modifications do not affect the model behavior in the viscous sublayer and buffer layer, we extracted the variation of dimensionless velocity U^+ in a flat plate computation, as illustrated in Figure 4.4.

4.2 Results and Discussion

Next, the WA2018SU, WA2018S-1, and WA2018S-2 models are subjected to the same test cases given in Section 3.2, and their results are presented in this section

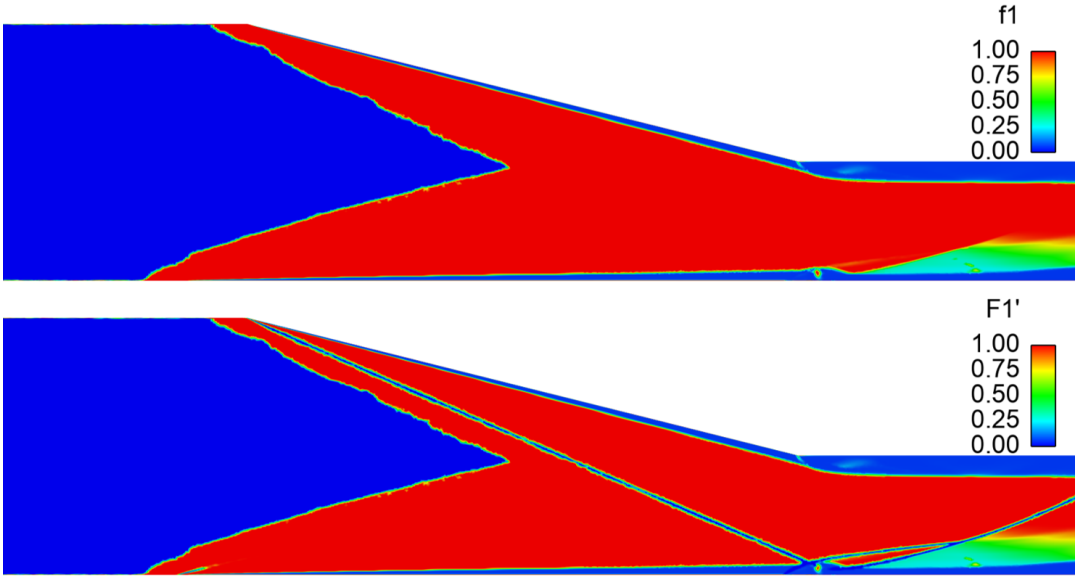

Figure 4.3: f_1 vs. $F_1^{'}$ in Schulein impinging shock test case

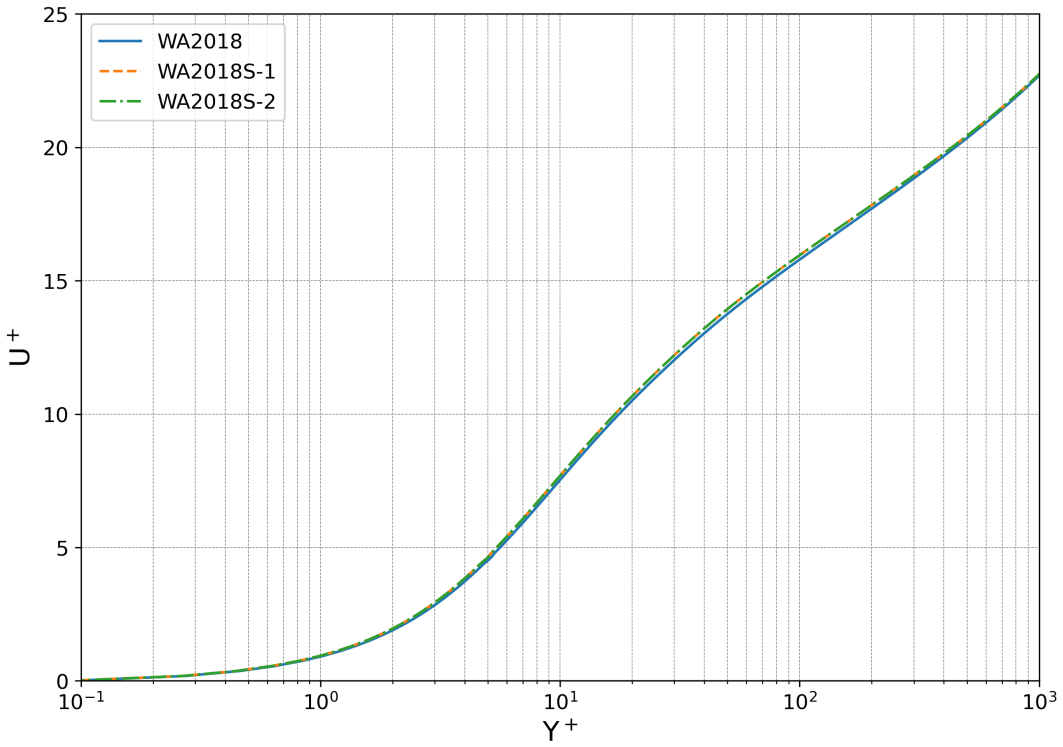

Figure 4.4: Variation of U^+ across the boundary layer

alongside the standard WA2018 model. The WA2018SU abbreviation corresponds to the shock unsteadiness modification given in Section 4.1.1. Also, the WA2018S-1 and WA2018S-2 indicate the modifications given in Eqs. (4.4) and (4.5), respectively.

4.2.1 Settles' Test Case

Starting from the Settles' 24^o compression ramp test case, the normalized wall pressure and skin friction coefficient distribution results of the modified and standard WA2018 models are presented in Figure 4.5. The modified WA2018 models produce later separation and smaller recirculation zones compared to the standard WA2018 model. The WA2018S-1 and WA2018S-2 models provide almost the same results, which are slightly better than the WA2018SU model results. Even though differences are minimal in both wall pressure and skin friction coefficient distributions, the modified versions are closer to the experimental data than the standard WA2018 model in the separation region.

4.2.2 Schulein's Test Case

In the Schulein impinging shock test case, the results of the modifications are investigated for three different shock generator angles, which are given in Figure 4.6 and 4.7. For all shock generator angle test cases, the WA2018SU model gives very similar distributions as the standard model, whereas the Reynolds anisotropy modifications result in slightly later separation. However, no significant alteration in the behavior is observed for any modification methodology in Schulein's impinging shock problem.

4.2.3 Holden's Test Case

The results of the modified WA2018 models, alongside the standard version for Holden's hypersonic compression ramp test case, are presented for 27^o and 36^o ramp angles in Figure 4.8 and 4.9 respectively. The most obvious differences are observed in this case. In the 27^o ramp angle case of Holden's test case, the Reynolds anisotropy modifications predict very similar wall pressure and shear stress distributions as the

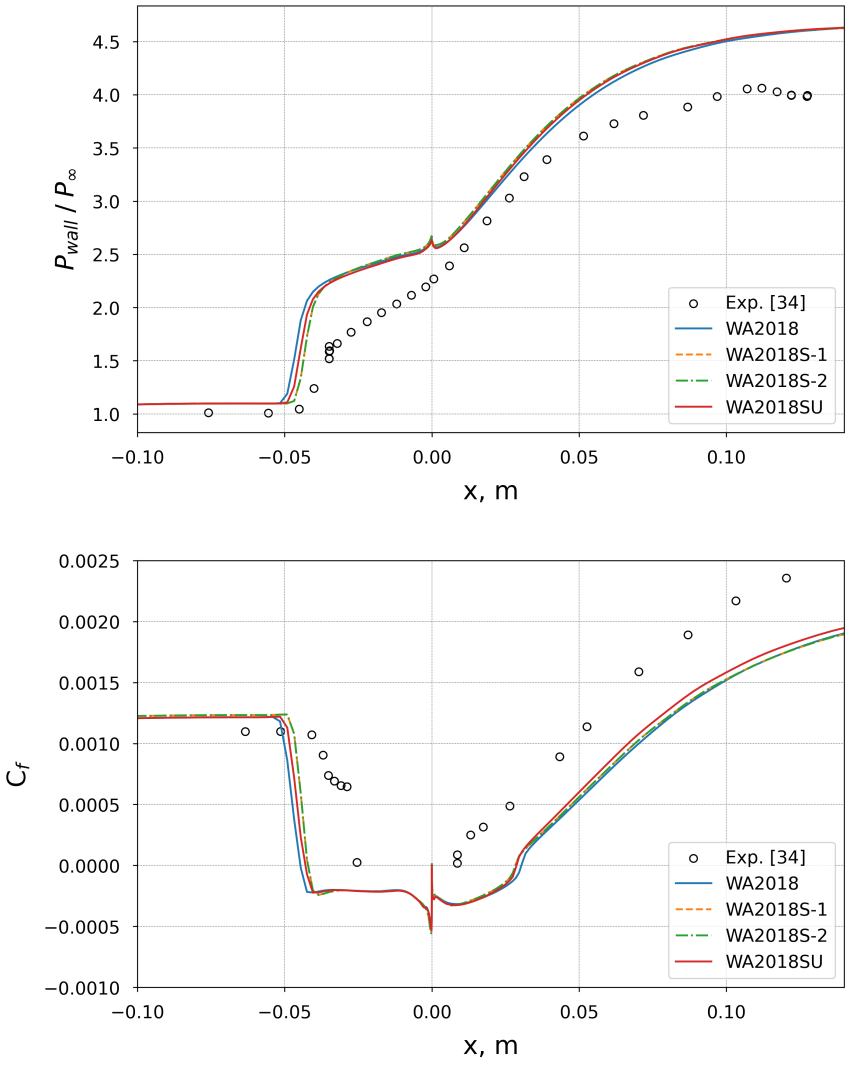

Figure 4.5: Modified models' results on Settles 24^o compression ramp test case

standard WA2018 model, which are both in line with the experimental data. However, the WA2018SU model predicts an unphysical separation, as seen in Figure 4.8. In the case of 36^o ramp angle, the WA2018SU model performs an earlier separation, which worsens the agreement with the experiment for both wall pressure and shear stress distributions. On the other hand, the WA2018S-1 and WA2018S-2 solutions match with the experimental data well for 36^o ramp angle case. Therefore, by looking at the results in Figure 4.9, it can be said that the Reynolds anisotropy-modified versions are superior to the shock unsteadiness modified and standard model versions in Holden's hypersonic compression ramp.

4.2.4 Kussoy's Test Case

The changes are negligible for Kussoy's impinging shock test case, as seen in Figure 4.10. All the modified versions of the WA2018 model still fail to catch the separation in this flow. On the other hand, the modifications do not worsen the behavior of the standard WA2018 model.

After examining the modified models' results, turbulent kinetic energy, k, distributions across the shock waves are acquired from the post-process for each case. Figure 4.11 demonstrates turbulent kinetic energy distributions starting from upstream of shock waves.

In Settles' test case, the modifications make insignificant differences in the k distributions while the maximum value is unchanged. For Schulein's test case, the anisotropy modification and standard WA2018 distributions are on top of each other, where the WA2018SU model predicts very high turbulent kinetic energy. Similar behavior is also seen in Holden's test case. The SU modification is expected to suppress the turbulent kinetic energy across shock waves; on the contrary, it increases for Schulein and Holden's test cases.

The effect of the SU modification on the WA model is not similar to those in Sinha's $k-\varepsilon$ and SA model modifications [11, 25]. The anisotropy modification, on the other hand, results insignificant changes in turbulent kinetic energy distributions. Therefore, the anisotropy modification affects the model via turbulent boundary layers.

4.3 Effect of the Modifications on the Heat Flux Predictions

As mentioned in Section 3.2.2, the Wray-Agarwal models provide excessive heat flux predictions. After the modifications are applied to the WA2018 model, the heat flux predictions are investigated, and their results are given in this section. Figure 4.12 demonstrates that the application of the modifications led to insignificant effects on the heat flux predictions. Therefore, further investigations are still required to find the reason behind this overprediction trend.

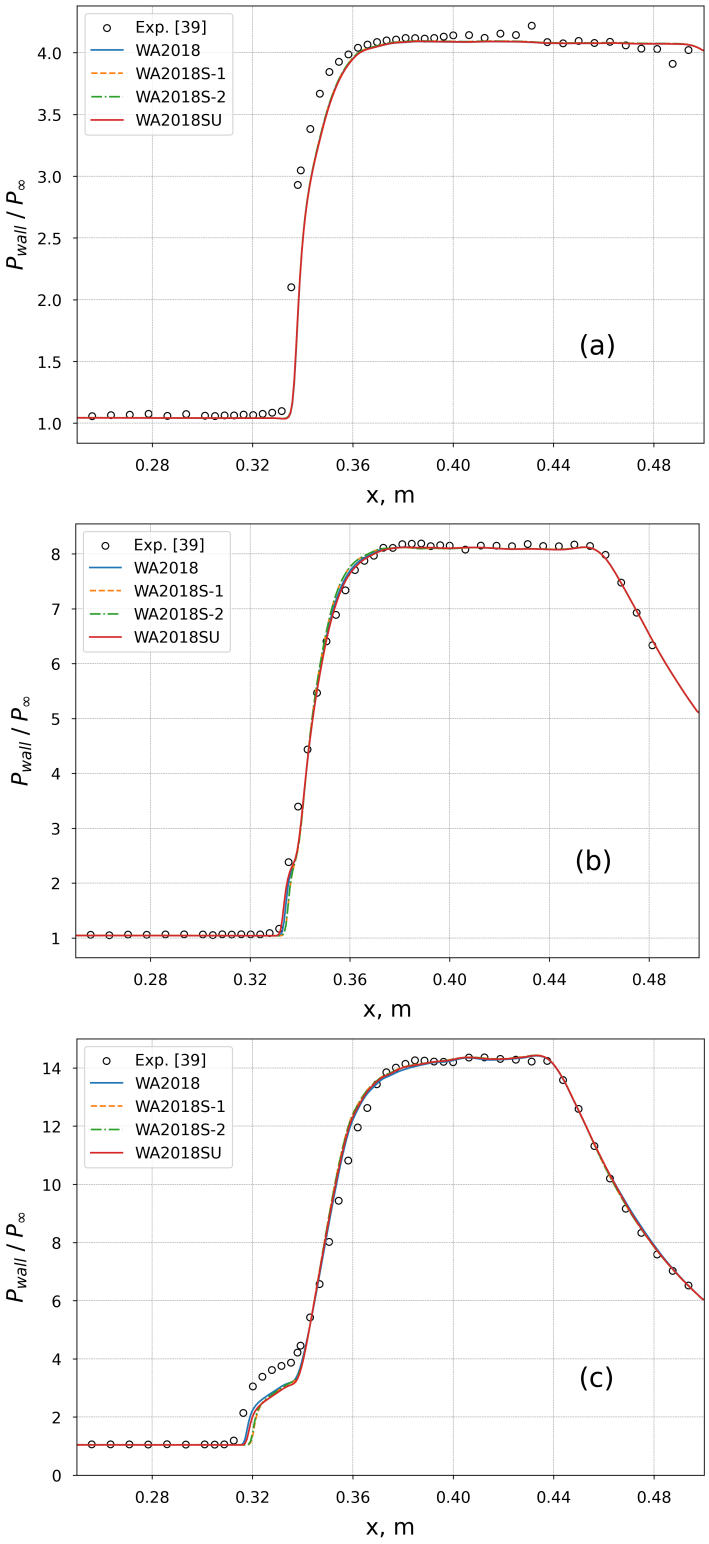

Figure 4.6: Modified models' pressure results on Schulein impinging shock test case for (a) $\beta = 6^o$, (b) $\beta = 10^o$, and (c) $\beta = 14^o$

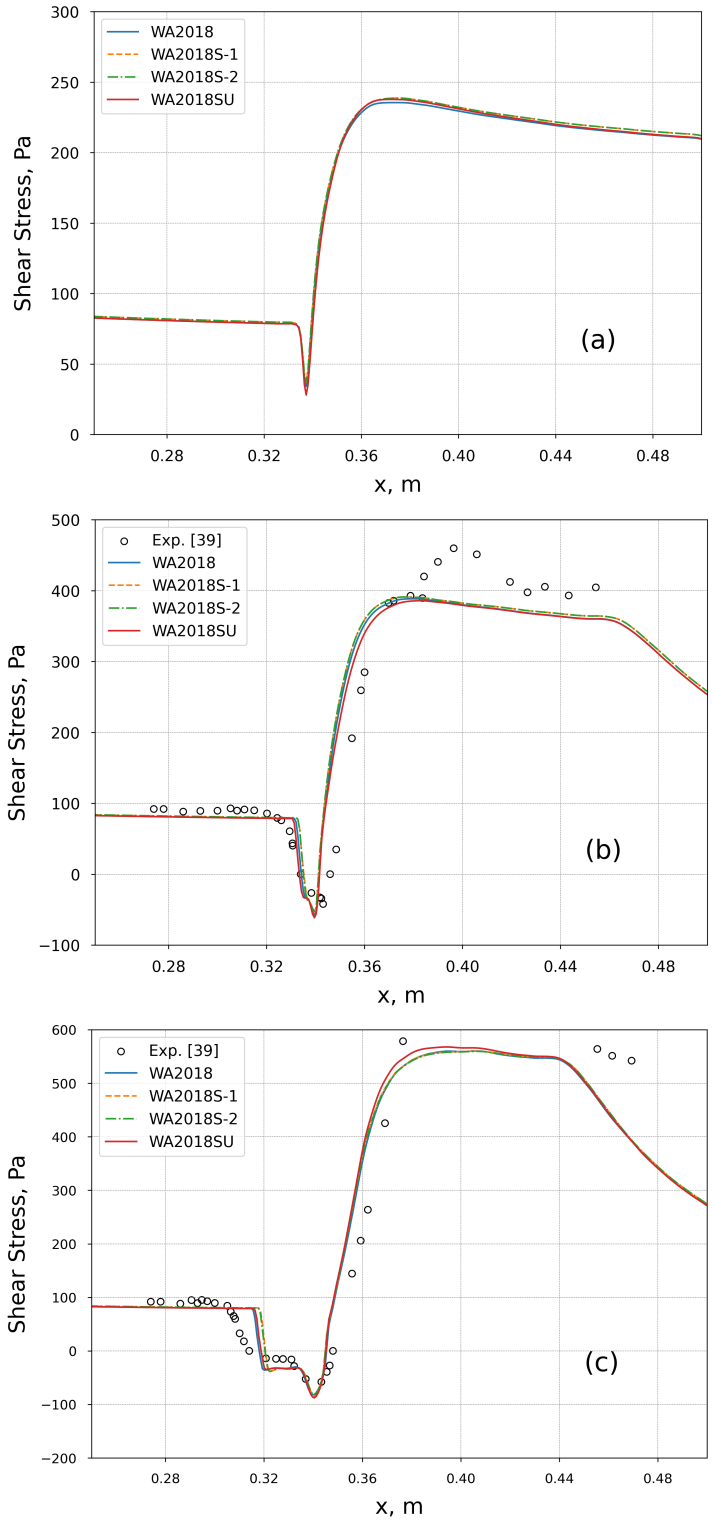

Figure 4.7: Modified models' shear stress results on Schulein impinging shock test case for (a) $\beta = 6^o$, (b) $\beta = 10^o$, and (c) $\beta = 14^o$

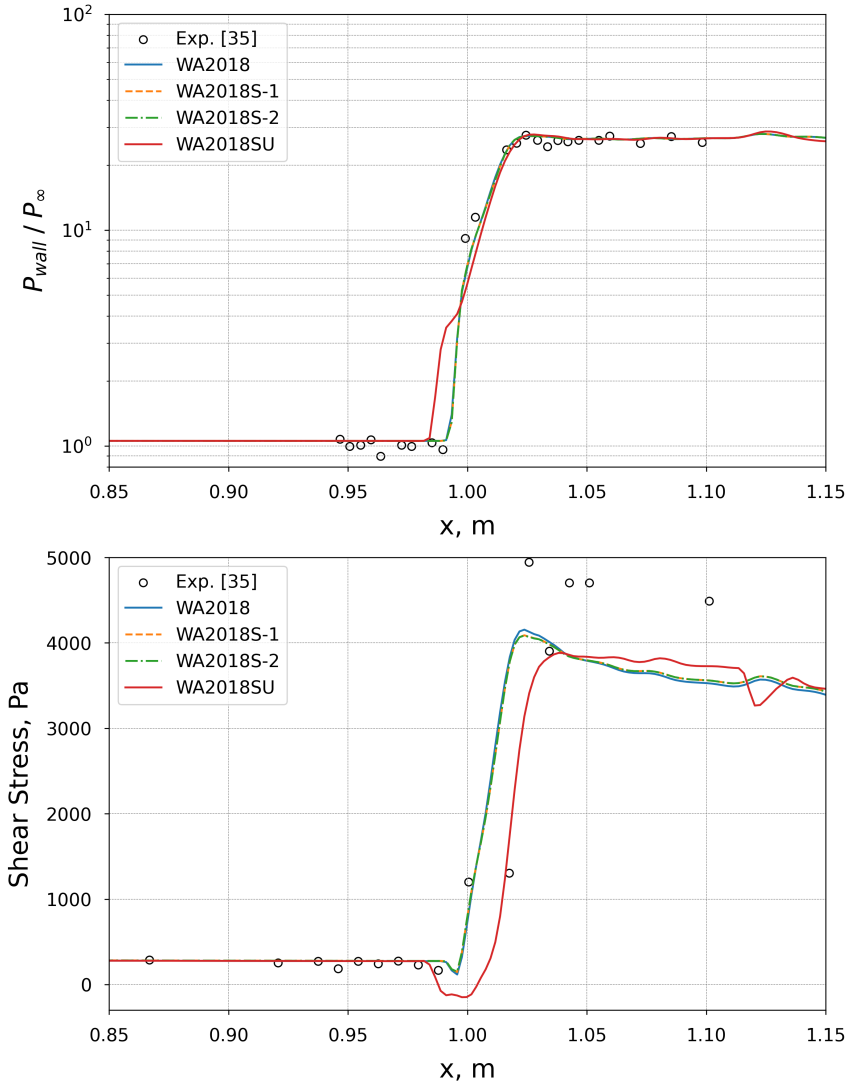

Figure 4.8: Modified models' results on Holden compression ramp test case for 27^o ramp angle

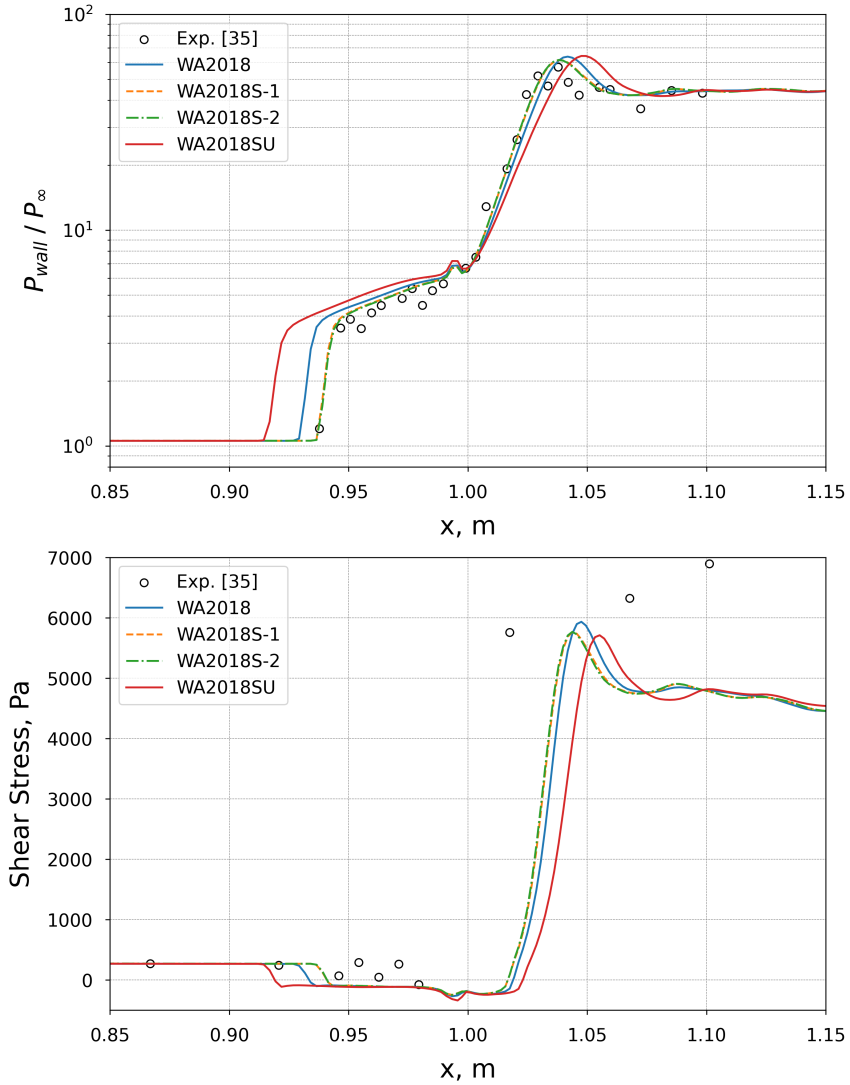

Figure 4.9: Modified models' results on Holden compression ramp test case for 36^o ramp angle

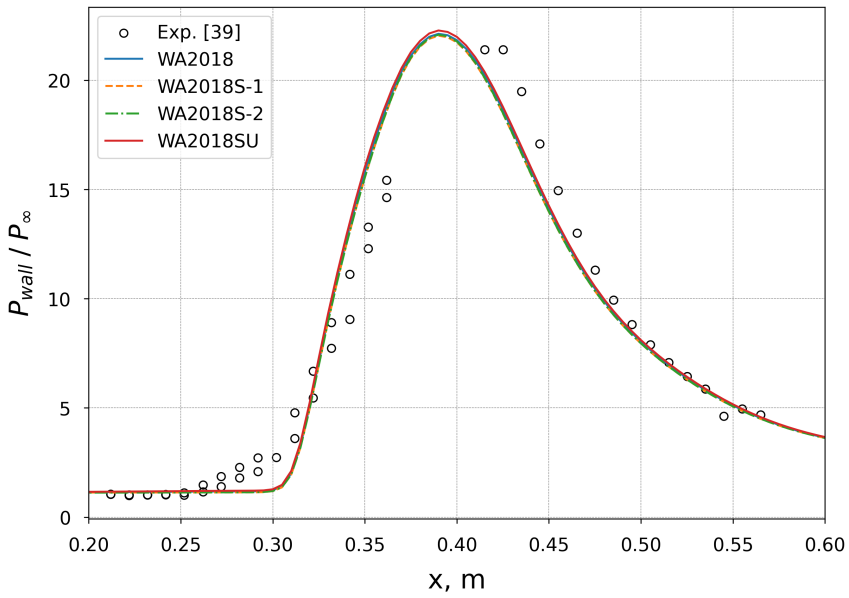

Figure 4.10: Modified models's results on Kussoy 10^o shock generator angle impinging shock test case

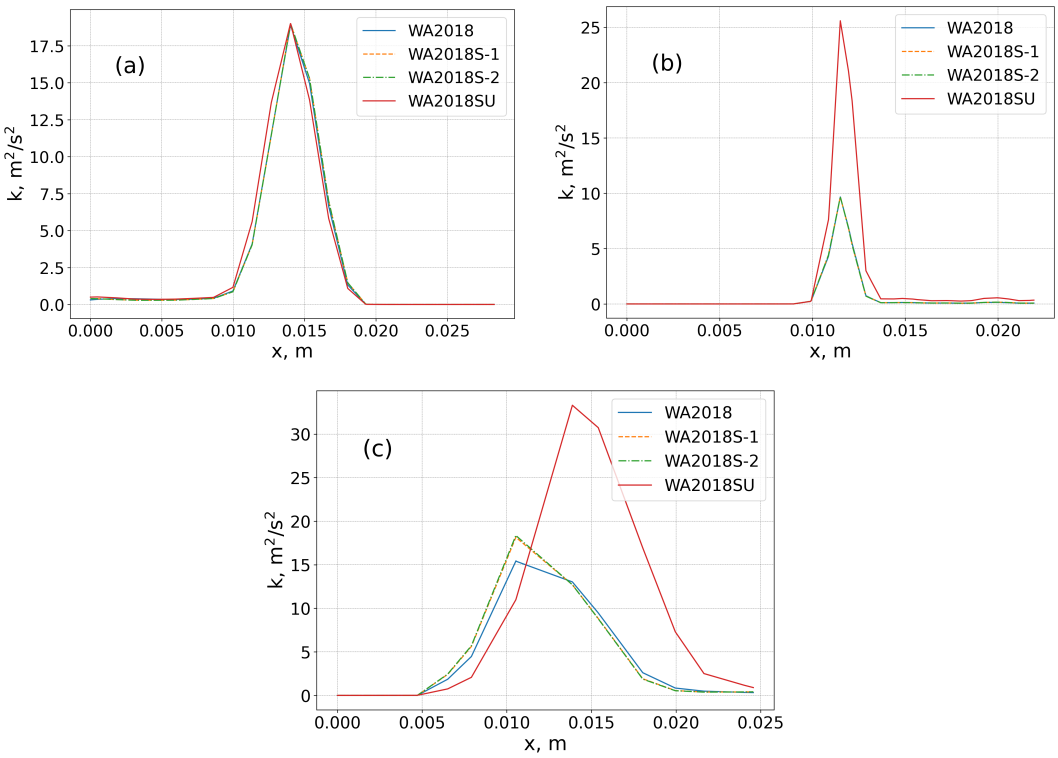

Figure 4.11: Distributions of turbulent kinetic energy, k, across shock waves on (a) Settles', (b) Schulein's, and (c) Holden's test cases

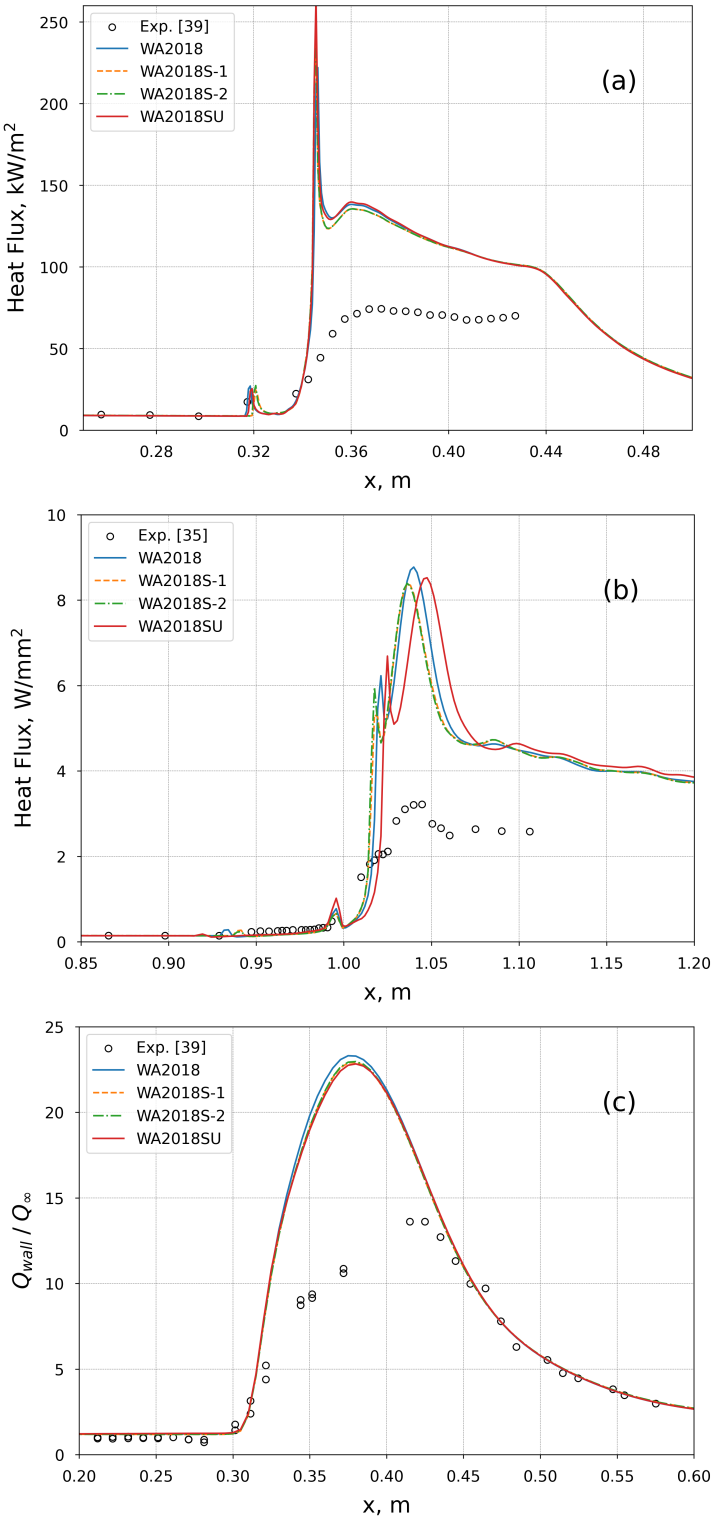

Figure 4.12: Modified models' heat flux results on (a) Schulein's 14^o, (b) Holden's 36^o, and (c) Kussoy's 10^o test cases

CHAPTER 5

CONCLUSION AND FUTURE WORK

In this study, the Wray-Agarwal 2017 and 2018 turbulence models are implemented into the open-source CFD solver, $flowPsi$. After implementations were verified using flat plate, wall-mounted hump, and backward-facing step cases, the WA 2017 and 2018 models were subjected to a validation study in the context of SWBLI flows. For this reason, four different test cases were selected with compression ramp- and impinging shock-type problems from literature with a flow regime ranging between Mach numbers from 2.84 to 8.2.

The results of the validation study are discussed in Section 3.2 as an assessment of the WA model in SWBLI flows. It is concluded that the WA model outperforms the SA model for impinging shock-type flows. Thus, the industrial usage of the WA models is advised for supersonic and hypersonic intakes. For compression ramp-type problems, the WA2018 model performs similarly to the SA model, whereas the WA2017 model fails. Also, the WA models perform insufficiently in terms of heat flux calculations.

This thesis also includes two different types of modifications to the WA2018 model. In the first modification attempt, the SU model by Sinha et al. is applied to the WA2018 model. The model's behavior degrades for the hypersonic compression ramp flow despite the fact that this alteration has negligible impacts on the supersonic compression ramp and hypersonic impinging shock problems. Therefore, the implementation of the SU model by Sinha et al. to the WA2018 model does not improve the model's performance in the context of SWBLI flows.

As a second modification, we developed WA2018S models from the standard WA2018 model. We performed this alteration in a way similar to the SUQ-SST model by Raje

and Sinha. The predictions obtained with the new anisotropy-included versions of the WA2018 model are in better agreement with the experiments compared to the standard WA2018 model. The inclusion of Reynolds stress anisotropy into the turbulent boundary layer improves the predictions significantly, as observed in both WA2018S-1 and WA2018S-2 results. We also observed that the WA2018S-2 model produces consistently almost identical distributions as WA2018S-1, which shows that introducing the Reynolds stress anisotropy specifically in the vicinity of shock waves does not lead to sensible differences in the results. Therefore, the use of WA2018S-1 instead of WA2018S-2 is recommended for SWBLI flows since there are fewer computations in the WA2018S-1 model because of the lack of function f_s.

It is evident that the eddy viscosity estimation based on the anisotropy parameter (C_μ^*) does not worsen the predictions of the impinging shock cases. Nevertheless, it produces more realistic shock-induced separations for compression corner-type problems where the standard WA2018 model falls behind the SA model. Thus, the new WA2018S-1 formulation is concluded to be a better alternative for SWBLI flows.

The WA models tested in this study showed poor performance in the prediction of heat fluxes after separation in hypersonic compression corners and impinging shock test cases. For this reason, CFD practitioners should be careful when using WA-based models in computations where thermal effects are important. In future work, this inadequate behavior should be investigated and improved for the SWBLI flows. For this purpose, the first layer thickness would be analyzed to see its effect on the heat flux distributions.

REFERENCES

[1] J. Blazek, *Computational Fluid Dynamics: Principles and applications*. Butterworth Heinemann, 2015.

[2] K. Duraisamy, G. Iaccarino, and H. Xiao, "Turbulence modeling in the age of data," *Annual Review of Fluid Mechanics*, vol. 51, p. 357–377, Jan 2019.

[3] T. J. Wray and R. K. Agarwal, "Low-reynolds-number one-equation turbulence model based on k-ω closure," *AIAA Journal*, vol. 53, pp. 2216–2227, Aug 2015.

[4] D. C. Wilcox, "Formulation of the k-w turbulence model revisited," *AIAA Journal*, vol. 46, p. 2823–2838, Nov 2008.

[5] E. Fares and W. Schröder, "A general one-equation turbulence model for free shear and wall-bounded flows," *Flow, Turbulence and Combustion*, vol. 73, p. 187–215, Jan 2005.

[6] T. Wray and R. K. Agarwal, "Application of the wray-agarwal model to compressible flows," *46th AIAA Fluid Dynamics Conference*, Jun 2016.

[7] X. Han, M. Rahman, and R. K. Agarwal, "Development and application of wall-distance-free wray-agarwal turbulence model (wa2018)," *2018 AIAA Aerospace Sciences Meeting*, Jan 2018. AIAA 2018-0593.

[8] F. Acquaye, J. Li, T. Wray, and R. K. Agarwal, "Validation of the wray-agarwal turbulence model for shock-wave boundary layer interaction flows," *46th AIAA Fluid Dynamics Conference*, Jun 2016. AIAA 2016-3477.

[9] H. Babinsky and J. Harvey, *Shock wave boundary layer interactions*. Cambridge University Press, 2011.

[10] G. V. Candler, P. K. Subbareddy, and J. M. Brock, "Advances in computational fluid dynamics methods for hypersonic flows," *Journal of Spacecraft and Rockets*, vol. 52, p. 17–28, Jan 2015.

[11] K. Sinha, K. Mahesh, and G. V. Candler, "Modeling shock unsteadiness in shock/turbulence interaction," *Physics of Fluids*, vol. 15, p. 2290–2297, Aug 2003.

[12] F. Thivet, D. D. Knight, A. A. Zheltovodov, and A. I. Maksimov, "Insights in turbulence modeling for crossing-shock-wave/boundary-layer interactions," *AIAA Journal*, vol. 39, p. 985–995, Jun 2001.

[13] F. R. Menter, "Two-equation eddy-viscosity turbulence models for engineering applications," *AIAA Journal*, vol. 32, p. 1598–1605, Aug 1994.

[14] F. R. Menter, "A comparison of some recent eddy-viscosity turbulence models," *Journal of Fluids Engineering*, vol. 118, p. 514–519, Sep 1996.

[15] W. W. Liou, G. Huang, and T.-H. Shih, "Turbulence model assessment for shock wave/turbulent boundary-layer interaction in transonic and supersonic flows," *Computers and Fluids*, vol. 29, p. 275–299, Mar 2000.

[16] D. Tang, J. Li, F. Zeng, Y. Li, and C. Yan, "Bayesian parameter estimation of sst model for shock wave-boundary layer interaction flows with different strengths," *Chinese Journal of Aeronautics*, vol. 36, p. 217–236, Apr 2023.

[17] J. Tan and J. Jin, "Stress limiter consideration for k-omega turbulence models in shock-wave/turbulent boundary-layer interactions in supersonic and hypersonic flows," *20th AIAA Computational Fluid Dynamics Conference*, Jun 2011. AIAA 2011-3980.

[18] N. Georgiadis and D. Yoder, "Recalibration of the shear stress transport model to improve calculation of shock separated flows," *51st AIAA Aerospace Sciences Meeting including the New Horizons Forum and Aerospace Exposition*, Jan 2013. AIAA 2013-0685.

[19] P. Raje and K. Sinha, "Anisotropic sst turbulence model for shock-boundary layer interaction," *Computers and Fluids*, vol. 228, p. 105072, Oct 2021.

[20] T. Rung, H. Lübcke, M. Franke, L. Xue, F. Thiele, and S. Fu, "Assessment of explicit algebraic stress models in transonic flows," *Engineering Turbulence Modelling and Experiments 4*, p. 659–668, 1999.

[21] X. Zhang, T. Wray, and R. K. Agarwal, "Application of a new simple rotation and curvature correction to the wray-agarwal turbulence model," *46th AIAA Fluid Dynamics Conference*, Jun 2016. AIAA 2016-3475.

[22] X. Han, T. Wray, and R. K. Agarwal, "A new des model based on wray-agarwal turbulence model for simulation of wall boundeed flows," *55th AIAA Aerospace Sciences Meeting*, Jan 2017. AIAA 2017-0979.

[23] H. Nagapetyan and R. K. Agarwal, "Development of a new transitional flow model integrating the wray-agarwal turbulence model with an intermittency transport equation," *2018 Fluid Dynamics Conference*, Jun 2018. AIAA 2018-3384.

[24] C. L. Rumsey, "Turbulence modeling resource," *https://turbmodels.larc.nasa.gov/*, 2024. (Accessed on 06/06/2024).

[25] K. Sinha, "Shock unsteadiness model applied to hypersonic shock-wave/turbulent boundary layer interactions," *44th AIAA Aerospace Sciences Meeting and Exhibit*, Jan 2006. AIAA 2006-126.

[26] E. A. Luke, X. Tong, and R. Chamberlein, "Flowpsi source code, version 1-0-p6," 2023.

[27] E. A. Luke and T. George, "Loci: A rule-based framework for parallel multi-disciplinary simulation synthesis," *Journal of Functional Programming*, vol. 15, p. 477–502, May 2005.

[28] E. A. Luke, X. Tong, and R. Chamberlain, *FlowPsi: An ideal gas flow solver - The User Guide*. 2023.

[29] E. F. Toro, M. Spruce, and W. Speares, "Restoration of the contact surface in the hll-riemann solver," *Shock Waves*, vol. 4, p. 25–34, Jul 1994.

[30] V. Venkatakrishnan, "On the accuracy of limiters and convergence to steady state solutions," *31st Aerospace Sciences Meeting*, Jan 1993. AIAA 93-0880.

[31] E. Dikbas, *Developments on capabilities of open-source compressible flow solvers for wall-bounded separated flows*. PhD thesis, METU, 2023.

[32] U. C. Ayan, "Implementation and assessment of the generalized riemann problem method in an unstructured solver," Master's thesis, METU, 2022.

[33] M. Park, B. Lee-Rausch, and C. Rumsey, "Fun3d and cfl3d computations for the first high lift prediction workshop," *49th AIAA Aerospace Sciences Meeting including the New Horizons Forum and Aerospace Exposition*, Jan 2011.

[34] G. S. Settles, I. E. Vas, and S. M. Bogdonoff, "Details of a shock-separated turbulent boundary layer at a compression corner," *AIAA Journal*, vol. 14, p. 1709–1715, Dec 1976.

[35] M. S. Holden, T. P. Wadhams, and M. G. MacLean, "Measurements in regions of shock wave/turbulent boundary layer interaction from mach 4 to 10 for open and "blind" code evaluation/validation," *21st AIAA Computational Fluid Dynamics Conference*, Jun 2013. AIAA 2013-2836.

[36] D. Knight, H. Yan, A. G. Panaras, and A. Zheltovodov, "Advances in cfd prediction of shock wave turbulent boundary layer interactions," *Progress in Aerospace Sciences*, vol. 39, p. 121–184, Feb 2003.

[37] E. Schülein, "Skin friction and heat flux measurements in shock/boundary layer interaction flows," *AIAA Journal*, vol. 44, p. 1732–1741, Aug 2006.

[38] M. Kussoy, G. Huang, and F. Menter, *Hypersonic Flows as Related to the National Aerospace Plane*. NASA Ames Research Center NASA CR-199365, 1995.

[39] J. G. Marvin, J. L. Brown, and P. A. Gnoffo, *Experimental Database with Baseline CFD Solutions: 2-D and Axisymmetric Hypersonic Shock-Wave/Turbulent-Boundary-Layer Interactions*. NASA Ames Research Center NASA TM-2013-216604, 2013.

[40] M. A. Leschziner, "Modelling turbulent separated flow in the context of aerodynamic applications," *Fluid Dynamics Research*, vol. 38, p. 174–210, Feb 2006.

[41] P. Spalart and S. Allmaras, "A one-equation turbulence model for aerodynamic flows," *30th Aerospace Sciences Meeting and Exhibit*, Jan 1992. AIAA 92-0439.

[42] D. C. Wilcox, “Reassessment of the scale-determining equation for advanced turbulence models,” *AIAA Journal*, vol. 26, p. 1299–1310, Nov 1988.

[43] T. B. Gatski and C. G. Speziale, “On explicit algebraic stress models for complex turbulent flows,” *Journal of Fluid Mechanics*, vol. 254, p. 59–78, Sep 1993.

[44] J. Forsythe, K. Hoffmann, and H.-M. Damevin, “An assessment of several turbulence models for supersonic compression ramp flow,” *29th AIAA, Fluid Dynamics Conference*, Jun 1998. AIAA 98-2648.